OPEN ACCESS



Shock Cooling and Breakout Emission for Optical Flares Associated with Gravitationalwave Events

Hiromichi Tagawa 1 , Shigeo S Kimura 2,3 , Zoltán Haiman 4,5 , Rosalba Perna 6,7 , and Imre Bartos 8 , Shanghai Astronomical Observatory, Shanghai, 200030, People's Republic of China; htagawa@shao.ac.cn 2 Astronomical Institute, Graduate School of Science, Tohoku University, Aoba, Sendai 980-8578, Japan 3 Frontier Research Institute for Interdisciplinary Sciences, Tohoku University, Sendai 980-8578, Japan 4 Department of Astronomy, Columbia University, 550 W. 120th St., New York, NY 10027, USA 5 Department of Physics, Columbia University, 550 W. 120th St., New York, NY 10027, USA 6 Department of Physics and Astronomy, Stony Brook University, Stony Brook, NY 11794-3800, USA 7 Center for Computational Astrophysics, Flatiron Institute, New York, NY 10010, USA 8 Department of Physics, University of Florida, P.O. Box 118440, Gainesville, FL 32611, USA Received 2023 October 27; revised 2024 January 22; accepted 2024 February 21; published 2024 April 23

Abstract

The astrophysical origin of stellar-mass black hole (BH) mergers discovered through gravitational waves (GWs) is widely debated. Mergers in the disks of active galactic nuclei (AGNs) represent promising environments for at least a fraction of these events, with possible observational clues in the GW data. An additional clue to unveil AGN merger environments is provided by possible electromagnetic emission from postmerger accreting BHs. Associated with BH mergers in AGN disks, emission from shocks emerging around jets launched by accreting merger remnants is expected. Here we compute the properties of the emission produced during breakout and the subsequent adiabatic expansion phase of the shocks, and we then apply this model to optical flares suggested to be possibly associated with GW events. We find that the majority of the reported flares can be explained by breakout and shock cooling emission. If the optical flares are produced by shock cooling emission, they would display moderate color evolution, possibly color variations among different events, and a positive correlation between delay time and flare duration and would be preceded by breakout emission in X-rays. If the breakout emission dominates the observed lightcurve, we predict the color to be distributed in a narrow range in the optical band and the delay time from GW to electromagnetic emission to be longer than ~2 days. Hence, further explorations of delay time distributions, flare color evolution, and associated X-ray emission will be useful to test the proposed emission model for the observed flares.

Unified Astronomy Thesaurus concepts: Astrophysical black holes (98); Gravitational wave sources (677); Active galactic nuclei (16); Transient sources (1851); Jets (870)

1. Introduction

The astrophysical pathways to black hole (BH) mergers discovered by the LIGO (LIGO Scientific Collaboration et al. 2015), Virgo (Acernese et al. 2015), and KAGRA (Akutsu et al. 2021) gravitational-wave (GW) observatories have been actively debated (Barack et al. 2019). Various scenarios have been proposed, including isolated binary evolution (e.g., Dominik et al. 2012; Kinugawa et al. 2014; Belczynski et al. 2016; Tagawa et al. 2018; Spera et al. 2019; Tanikawa et al. 2022) evolution of triple or quadruple systems (e.g., Antonini et al. 2017; Silsbee & Tremaine 2017; Fragione & Kocsis 2019; Michaely & Perets 2019; Martinez et al. 2022; Bartos et al. 2023), dynamical evolution in star clusters (e.g., Portegies Zwart & McMillan 2000; Samsing et al. 2014; O'Leary et al. 2016; Rodriguez et al. 2016; Banerjee 2017; Fragione & Kocsis 2018; Kumamoto et al. 2018; Perna et al. 2019; Rasskazov & Kocsis 2019; Antonini et al. 2023), and compact objects in active galactic nucleus (AGN) disks (e.g., Bartos et al. 2017; Stone et al. 2017; McKernan et al. 2018; Tagawa et al. 2020b; Arca Sedda et al. 2023).

Original content from this work may be used under the terms of the Creative Commons Attribution 4.0 licence. Any further distribution of this work must maintain attribution to the author(s) and the title of the work, journal citation and DOI.

In an AGN disk, BHs are embedded due to capture via dynamical interactions between the nuclear star cluster and the AGN disk (Ostriker 1983; Miralda-Escudé & Kollmeier 2005; Generozov & Perets 2023; Wang et al. 2024) and by in situ star formation (Levin & Beloborodov 2003; Goodman & Tan 2004; Milosavljević & Loeb 2004; Chen et al. 2023b; Derdzinski & Mayer 2023). The AGN disk environment helps to bring the BHs closer together (Bellovary et al. 2016; Derdzinski et al. 2019, 2021; Tagawa et al. 2020b; Li et al. 2021; Grishin et al. 2023) and hence form binaries (Li et al. 2022, 2023; Boekholt et al. 2023; DeLaurentiis et al. 2023; Qian et al. 2024; Rowan et al. 2023, 2024; Rozner et al. 2023; Whitehead et al. 2023a; Whitehead et al. 2023b), which then merge over relatively short timescales. Comparisons to the observed BH masses, spins, and merger rate indicate that a sizable fraction of the observed mergers may indeed originate in AGN disks (Tagawa et al. 2021a; Gayathri et al. 2021; Ford & McKernan 2022). The AGN channel could also explain some of the peculiar detections, such as those with a high mass (Tagawa et al. 2021a; Gayathri et al. 2023) and possibly high eccentricity (Tagawa et al. 2021b; Gayathri et al. 2022; Romero-Shaw et al. 2022; Samsing et al. 2022; but see Romero-Shaw et al. 2020, 2023).

Due to the gas-rich merger environment, a key signature of the AGN channel is the possibility of electromagnetic emission accompanying the GW signal from the merger (Bartos et al. 2017; Stone et al. 2017). To explore this possibility,

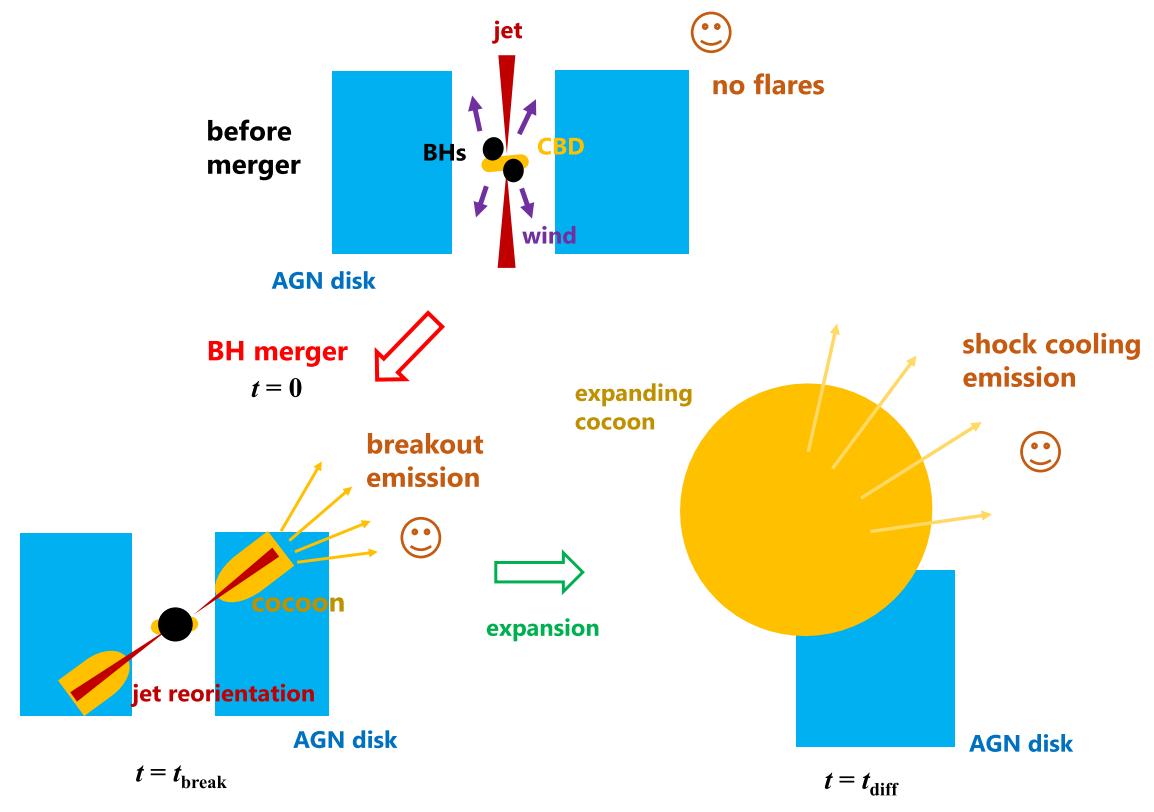


Figure 1. A schematic picture of breakout and cooling envelope emission from shocks produced by the interaction of AGN gas and a jet launched from a BH accreting gas in an AGN disk. Since the jet is reoriented at the time of the merger of two BHs (Section 2.1), electromagnetic emission is also produced after the merger.

electromagnetic follow-up observations have been carried out for many of the mergers, with nine counterpart candidates suggested so far, including seven optical flares (Graham et al. 2020, 2023) and two gamma-ray flares (Bagoly et al. 2016; Connaughton et al. 2016).

Recently, several studies have investigated the electromagnetic emission from a variety of transients emerging from AGN disks. Many studies (Perna et al. 2021a; Yuan et al. 2022; Zhu et al. 2021a, 2021c; Lazzati et al. 2022; Wang et al. 2022; Ray et al. 2023) focused on the radiation from gamma-ray bursts, while Perna et al. (2021b) and Zhu et al. (2021b) discussed the electromagnetic signatures expected from accretion-induced collapse of neutron stars and white dwarfs, respectively. Yang et al. (2022), Xin et al. (2024), and Prasad et al. (2023) studied the properties of tidal disruption of stars by BHs, while Grishin et al. (2021) investigated supernova explosions, and Bartos et al. (2017) and Stone et al. (2017) estimated the electromagnetic emission produced by thermal radiation and/or outflow from circumbinary disks in AGN disks.

Several recent studies have also investigated whether transients from BHs merging in AGN disks could explain the optical flare, ZTF 19abanrhr (Graham et al. 2020), associated with the BH merger GW190521 detected in GWs. McKernan et al. (2019) discussed emission from shocks caused by collisions between gas bound to the merger remnant and unbound gas after recoil kicks due to anisotropic radiation of GWs. Graham et al. (2020) assessed the net luminosity and timescales for gas accretion induced by recoil kicks. De Mink & King (2017) considered flares emerging from shocks in a circum-BH disk due to recoil kicks. Kimura et al. (2021),

Wang et al. (2021a, 2021b), and Chen et al. (2023a), respectively, considered thermal and nonthermal emission from bubbles and bubble evolution around BHs formed by strong outflows considering continuous and episodic super-Eddington accretion. Wang et al. (2021a) further considered emission from shocks emerging due to interactions of Blandford–Znajek jets (Blandford & Znajek 1977) launched from accreting BHs to the broad-line regions, Rodríguez-Ramírez et al. (2024) considered free–free and bound–free emission from gas shocked due to interaction of the jets and AGN disk gas, and Tagawa et al. (2023a) estimated gammaray, neutrino, and cosmic-ray emission from internal shocks in the jets. Ashton et al. (2021), Calderón Bustillo et al. (2021), Palmese et al. (2021), and Morton et al. (2023) estimated the association significance of ZT F19abanrhr to GW190521.

In this paper, we develop an emission model based on the scenario proposed by Tagawa et al. (2022, 2023b) and discuss whether or not emission based on this scenario can explain some of the optical flares reported in Graham et al. (2023). Tagawa et al. (2022, hereafter T22) indicated that a Blandford-Znajek jet can be produced from BHs embedded in AGN disks and investigated its influence on the AGN disk structure. Due to the high pressure of the shocks emerging around the jet (or wind; Section 3.3), a cavity is created around the BHs. Just before the jet breaks out of the AGN disk, photons in the shocked gas begin to escape. These photons can be observed as breakout emission (e.g., Nakar & Sari 2010), whose properties have been investigated in Tagawa et al. (2023c). The BHs can maintain the jets even after they break out from the AGN disk, as long as there is leftover circum-BH disk gas. Once this is depleted, the BHs can no longer power the jets. This is then

 Table 1

 The Properties of the ZTF Flares Suggested to Be Associated with the GW Events

Pair	LIGO/Virgo Alert ID	Name of AGN	$\log_{10}\!\!\left(rac{M_{ m SMBH}}{M_{\odot}} ight)$	$m_{ m BH} \ (M_{\odot})$	t _{duration} (day)	t _{delay} (day)	$L_{\rm op}$ (erg s ⁻¹)	$L_{ m AGN}/L_{ m Edd}$
1	GW190403_051519	J124942.30+344928.9	8.6	111	45.3	89	44.9	0.06
2	GW190514_065416	J124942.30+344928.9	8.6	68	45.3	48	44.9	0.06
3	GW190521	J124942.30+344928.9	8.6	164	45.3	41	44.9	0.06
4	GW190403_051519	J183412.42+365655.3	9.1	111	41.0	110	43.8	0.02
5	GW190424_180648	J181719.94+541910.0	8.0	73	35.6	189	44.8	0.05
6	GW190514_065416	J224333.95+760619.2	8.8	68	18.3	154	45.2	0.06
7	GW190731_140936	J053408.41+085450.6	(8.0)	70.1	27.4	186	44.5	0.04
8	GW190803_022701	J053408.41+085450.6	(8.0)	65	27.4	183	44.5	0.04
9	GW190803_022701	J120437.98+500024.0	8.0	65	47.4	191	44.7	0.02
10	GW190909_114149	J120437.98+500024.0	8.0	75	47.4	154	44.7	0.02
11	GW200216_220804	J154342.46+461233.4	9.3	81	123.4	73	44.3	0.10
12	GW200220_124850	J154342.46+461233.4	9.3	67	123.4	69	44.3	0.10

Note. In each pair, the flare is located within the 90% credible volume and detected within the delay time of 200 days from the GW event. Here, $M_{\rm SMBH}$ is the SMBH mass, $m_{\rm BH}$ is the merged remnant mass, $t_{\rm duration}$ is the duration of the flare, $t_{\rm delay}$ is the delay time between the detection of the GWs and the flare, $L_{\rm op}$ is the optical luminosity of the flare, and $L_{\rm AGN}$ is the Eddington ratio of the host AGN. For J053408.41+085450.6, the SMBH mass is not constrained, and a fiducial mass of $10^8 M_{\odot}$ is used as in Graham et al. (2023).

followed by an inactive phase, which lasts until gas is replenished onto the BH and the jet is launched again, with the cycle hence repeating.

In the case where BHs merge in the cavity while accreting (upper panel of Figure 1), Tagawa et al. (2023b, hereafter Paper I) predicted that electromagnetic emission is often associated with the BH merger. This is because the jet direction can be reoriented following a merger (Section 2.1), and strong shocks and emission are produced soon after the jet reorientation. Paper I investigated the properties of breakout emission from a jet head associated with BH mergers and found that this model can explain various properties, including the luminosity, delay time, duration, and color of the electromagnetic transients ZTF 19abanrhr, GW150914-GBM, and LVT 151012, as well as why the transients began brightening only after the merger. Zhu (2024) and Zhou & Wang (2023) also estimated the neutrino emission from the breakout of the jets associated with BH mergers. In this paper, we additionally consider the shock cooling emission, which is produced in a subsequent adiabatic expansion phase of the shocked gas (e.g., Arnett 1980; Morag et al. 2023 for supernovae and Nakar & Piran 2017; Gottlieb et al. 2018; Hamidani & Ioka 2023 for gamma-ray bursts), in addition to the breakout emission, which is produced in an early phase of the shocked gas (see Figure 1 for a schematic picture). We present the properties of the emission in both phases, and we then apply this model to the flares reported in Graham et al. (2023). We further discuss how to test the proposed emission model in future observations.

The rest of this paper is organized as follows. In Section 2, we describe a model for producing electromagnetic flares associated with GW emission and a way to constrain the physical properties of the flares from the observations using

this model. We present our results in Section 3, discuss how to test the model in Section 4, and summarize our conclusions in Section 5.

2. Method

First we describe the model itself. We then specialize to discuss how to derive the model parameters from the observed properties of the flares, that is, the delay time (t_{delay}) , the duration ($t_{duration}$), the luminosity of the flare (L_{obs}), the merger remnant mass ($m_{\rm BH}$), the SMBH mass ($M_{\rm SMBH}$), and the AGN luminosity (L_{AGN}). In our analysis, we assume that the shocks produced by collisions between the jet and the AGN gas are characterized by nonrelativistic regimes. This is because in both the breakout and the shock cooling emission, flares with a delay time and duration of \gtrsim 10 days (Table 1) are usually characterized by this regime (Paper I; Tables 2 and 3). As possible processes for explaining the properties of the optical flares, we consider the breakout emission from the jet head (the breakout emission scenario) and shock cooling emission from the cocoon composed of the shocked AGN gas (the shock cooling emission scenario). Note that we use the Shakura-Sunyaev model (Shakura & Sunyaev 1973) for the accretion disk in the shock cooling emission scenario and the Thompson disk model (Thompson et al. 2005) in the breakout emission scenario. This is because the position of the BH from the central supermassive BH (SMBH) is subparsec for the former (Table 2) and a few parsecs for the latter case (Table 3), and the mechanisms of angular momentum transfer and the disk properties are likely different in the two regions, with the Thompson disk model better suited than the Shakura-Sunyaev one to describe the outer disk.

 Table 2

 The Inferred Model Parameters for the Shock Cooling Emission Scenario

Pair	R _{BH} (pc)	$R_{ m BH}\left(R_{ m g} ight)$	$\beta_{ m c}$	$h_{ m AGN}$	$ ho_{ m AGN} ho_{ m agn} ho_{ m agn}$	T _{BB} (K)	$\lambda_{ m peak} \ m (nm)$	$L_{\rm j}$ (erg s ⁻¹)	$f_{ m jet/BHL}$	t _{break} (days)	t _{diff,CBO} (Equation (28)) (s)
1	0.1	5×10^3	0.2	0.004	1×10^{-11}	1.4×10^{4}	350	1×10^{48}	40	0.9	200
2	0.1	5 × 10 ³	0.2	0.004	1×10^{-11}	1.4×10^{4}	350	1×10^{48}	50	0.9	200
3	0.1	5×10^3	0.2	0.004	1×10^{-11}	1.4×10^{4}	350	1×10^{48}	30	0.9	300
4	0.08	1×10^3	0.08	0.002	7×10^{-11}	1.4×10^{4}	350	1×10^{47}	2	0.8	200
5	0.1	3×10^4	0.2	0.005	1×10^{-12}	1.8×10^{4}	270	2×10^{47}	40	2	3×10^3
6	0.06	2×10^3	0.4	0.003	9×10^{-11}	1.3×10^{4}	380	2×10^{50}	3000	0.2	7
7	0.1	2×10^4	0.1	0.005	2×10^{-12}	1.9×10^{4}	250	2×10^{47}	30	1	2×10^3
8	0.1	2×10^4	0.1	0.005	2×10^{-12}	1.9×10^4	250	2×10^{47}	30	1	2×10^3
9	0.3	6×10^4	0.1	0.005	2×10^{-13}	2.0×10^{4}	240	5 × 10 ⁴⁶	20	6	5 × 10 ⁴
10	0.3	6×10^4	0.1	0.005	2×10^{-13}	2.0×10^{4}	240	5×10^{46}	20	6	5 × 10 ⁴
11	0.09	9×10^2	0.09	0.003	2×10^{-10}	9.2×10^{3}	520	8×10^{47}	5	1	60
12	0.09	9×10^2	0.09	0.003	2×10^{-10}	9.2×10^{3}	520	8×10^{47}	5	1	50

Note. $R_{\rm BH}$ is the distance from the SMBH to the BH; $\beta_{\rm c}$ is the expansion velocity of the shocked gas; $h_{\rm AGN} \equiv H_{\rm AGN}/R_{\rm BH}$ and $\rho_{\rm AGN}$ are the aspect ratio and the density of the AGN disk at the position of the BH, respectively; $T_{\rm BB}$ and $\lambda_{\rm peak}$ are the radiation temperature and wavelength of the shock cooling emission, respectively; $L_{\rm j}$ is the jet power; $f_{\rm jet/BHL}$ is a parameter related to the jet power; $t_{\rm break}$ is the breakout timescale of the jet; and $t_{\rm diff,CBO}$ is the diffusion timescale for the breakout emission from the shocked gas.

Table 3
The Inferred Model Parameters for the Breakout Emission Scenario

Pair	R _{BH} (pc)	β_{h}	$h_{ m AGN}$	ρ _{AGN} (g cm ⁻³)	$\dot{M}_{ m inflow}/\dot{M}_{ m Edd}$	$f_{ m op/kin}$	$f_{ m BH/NSC}$	$h_{ m AGN}/h_{ m AGN,TQM}$	f_{corr} for $h_{\text{AGN}} = h_{\text{AGN,TQM}}$
1	3.3	0.31	0.004	2×10^{-16}	0.06	0.36	0.38	1.05	3.1
2	3.5	0.33	0.002	1×10^{-16}	0.02	0.98	0.41	1.6	4.3
3	4.0	0.41	0.002	1×10^{-16}	0.01	0.73	0.46	1.5	4.2
4	4.5	0.29	0.004	2×10^{-16}	0.05	0.02	0.44	1.03	3.1
5	1.6	0.23	0.015	4×10^{-16}	0.9	0.11	0.23	1.4	4.0
6	2.4	0.23	0.008	7×10^{-16}	0.4	0.22	0.26	1.6	4.4
7	1.4	0.23	0.016	5×10^{-16}	1.2	0.05	0.21	1.6	4.3
8	1.4	0.22	0.016	5×10^{-16}	1.2	0.05	0.21	1.6	4.3
9	1.7	0.23	0.014	3×10^{-16}	0.7	0.14	0.25	1.3	3.7
10	1.8	0.25	0.011	3×10^{-16}	0.4	0.16	0.26	1.1	3.3
11	8.1	0.32	0.002	6×10^{-17}	0.004	0.34	0.74	2.0	5.2
12	8.0	0.31	0.001	6×10^{-17}	0.004	0.41	0.73	1.9	4.9

Note. $\dot{M}_{\rm inflow}/\dot{M}_{\rm Edd}$ is the Eddington ratio for the gas inflow at the position of the BH, $f_{\rm op/kin}$ is the fraction of the optical luminosity of the flare over the kinetic power of the jet, $f_{\rm BH/NSC}$ is the fraction of $R_{\rm BH}$ over the size of the nuclear star cluster, and $h_{\rm AGN}/h_{\rm AGN,TQM}$ is the ratio of the aspect ratio of the AGN disk derived from our model to that derived assuming the model in Thompson et al. (2005). In the last column, the value of the correction factor for the delay time, at which $h_{\rm AGN} = h_{\rm AGN,TQM}$ is satisfied, is listed.

2.1. Shock Formation

Shocked gas is responsible for both the breakout and the cooling emission, and hence we begin by describing the process of shock formation.

We first describe the accretion rate onto BHs in an AGN disk, which is evaluated by the Bondi–Hoyle–Lyttleton rate. For a BH embedded in a cool AGN disk, the Bondi–Hoyle–Lyttleton radius ($r_{\rm BHL}$) is large and usually exceeds the scale

height of the AGN disk ($H_{\rm AGN}$) and the Hill radius ($r_{\rm Hill}$). Accounting for the geometrical limitation of the capture regions by the shear motion and the vertical height of the AGN disk, the capture rate of gas by the BH is given by

$$\dot{m}_{\rm BHL} = f_{\rm c} r_{\rm w} r_{\rm h} \rho_{\rm AGN} (c_{\rm s, AGN}^2 + v_{\rm BH}^2 + v_{\rm sh}^2)^{1/2}$$

$$\simeq 3 \times 10^{-4} \, M_{\odot} \, \rm yr^{-1} \left(\frac{f_{\rm c}}{10} \right) \left(\frac{H_{\rm AGN}}{0.003 \, \rm pc} \right) \left(\frac{R_{\rm BH}}{1 \, \rm pc} \right)^{1/2}$$

$$\left(\frac{\rho_{\rm AGN}}{4 \times 10^{-17} \, \rm g \, cm^{-3}} \right) \left(\frac{m_{\rm BH}}{10 \, M_{\odot}} \right)^{2/3} \left(\frac{M_{\rm SMBH}}{10^6 \, M_{\odot}} \right)^{-1/6}$$
(1)

(e.g., Tanigawa & Tanaka 2016; Choksi et al. 2023), where ρ_{AGN} is the gas density, $c_{s,AGN}$ is the sound speed of the AGN disk at the position of the BH ($R = R_{BH}$, where R is the distance from the SMBH), v_{BH} is the velocity of the BH with respect to the local motion of the AGN disk, $v_{\rm sh} = r_{\rm w}\Omega$ is the shear velocity at the capture radius $r_{\rm w}=\min(r_{\rm BHL},\,r_{\rm Hill}),$ $\Omega = (GM_{\rm SMBH}/R_{\rm BH}^3)^{1/2}$ is the angular velocity of the BH, $r_{\rm h}={\rm min}(r_{\rm w},\,H_{\rm AGN})$ is the capture height, G is the gravitational constant, and $f_c \sim 10$ is a normalization constant (Tanigawa & Watanabe 2002). In the second line of Equation (1), we assume $v_{\rm BH} < c_{\rm s,AGN}$ and $v_{\rm BH} < v_{\rm sh}$. Note that $r_{\rm w}(c_{\rm s,AGN}^2 + v_{\rm sh}^2)^{1/2} \approx$ $r_{\text{Hill}}H_{\text{AGN}}\Omega$ is used to derive the right-hand side, which is approximately satisfied regardless of whether $c_{s,AGN}$ is larger or smaller than $v_{\rm sh}$. By considering the reduction or enhancement with respect to the Bondi-Hoyle-Lyttleton rate, we parameterize the fraction of the accretion rate onto the BH (\dot{m}) over the Bondi-Hoyle-Lyttleton rate ($\dot{m}_{\rm BHL}$) by $f_{\rm acc}=\dot{m}/\dot{m}_{\rm BHL}$ as in Paper I. For example, low f_{acc} may be predicted due to winds from an accretion disk with a super-Eddington rate (see Section 3.3). On the other hand, recent simulations suggest that the conversion to wind is moderate (Kitaki et al. 2021) for accretion flows in which the circularization radius (where gas is circularized after being captured by a BH) is much larger than the trapping radius (within which photons are advected to a BH without escaping), as is the case for BHs embedded in an AGN disk. In addition, the accretion rate onto a BH in a cavity during the active phases is estimated to be lower by a factor of a few compared to that without a cavity (T22).

From rapidly accreting and spinning BHs in an AGN disk, a Blandford–Znajek jet is expected to be launched, as outlined in Appendix A1 of T22. The jet kinetic luminosity (L_j) is proportional to the mass accretion rate onto the BH (\dot{m}) as

$$L_{\rm j} = \eta_{\rm j} \dot{m} c^2, \tag{2}$$

where c is the speed of light and $\eta_{\rm j}$ is the jet conversion efficiency, which is approximated by $\eta_{\rm j} \sim a_{\rm BH}^2$ for a magnetically dominated jet (Tchekhovskoy et al. 2010; Narayan et al. 2022), $a_{\rm BH}$ is the dimensionless spin of the BH, and $a_{\rm BH} \sim 0.7$ for the merger remnants (Abbott et al. 2023).

At a BH merger (t = 0, where t is the time from the merger), the jet direction is reoriented and can collide with unshocked AGN gas in the following ways. Once two BHs merge, the BH spin direction is reoriented if the angular momentum direction of the merging binary is misaligned with respect to the spin directions of the merging BHs. This is expected for mergers in an AGN disk due to frequent binary–single interactions (Tagawa et al. 2020a) and/or the inhomogeneity of AGN

disks. Since the jet is injected in the direction of the BH spin, if the jet is not aligned with the circum-BH disk due to a strong jet power (Polko & McKinney 2017), the jet propagates in the direction of the BH spin and can collide with AGN gas. Even if the jet aligns with the angular momentum direction of the circum-BH disk due to magnetic interactions, on average, the jet can precess by interacting with magnetic fields while the angular momentum directions of the BH spin and the circum-BH disk are still misaligned with one other (Liska et al. 2018, 2021). Due to the precession, the jet can collide with unshocked gas after the merger during the first precession cycle (after that, the opening angle of the cavity becomes wider than that of the precession). The other possibility is that once BHs merge, a merger remnant BH receives a recoil kick in an almost random direction due to anisotropic radiation of GWs. Then shocks form in a circum-BH disk within $\lesssim 10^{13}$ cm (Tagawa et al. 2023b), and shocked gas accretes onto the remnant with the angular momentum direction being modified as a result of shocks (Rossi et al. 2010). Due to magnetic interactions (Liska et al. 2021), the jet is then aligned with the angular momentum direction of the circum-BH disk, which is in turn misaligned with respect to the jet direction before the merger, and the jet can therefore collide with AGN gas.

Once the jet collides with unshocked AGN gas around a BH, two shocks form: a forward shock propagating in the AGN disk and a reverse shock in the jet. The region sandwiched by the two shocks is called the jet head. In the jet collimated regime considered in our work, the dimensionless velocity of shocked gas in the jet head at the shock breakout is estimated as (Bromberg et al. 2011)

$$\beta_{\rm h} \sim \left(\frac{L_{\rm j}}{\rho_{\rm AGN} t_{\rm break}^2 \theta_0^4 c^5}\right)^{1/5},\tag{3}$$

where θ_0 is the opening angle of the injected jet and t_{break} is the delay time between the production of the jet and the shock breakout, roughly given by

$$t_{\text{break}} \sim \frac{3}{5} \frac{H_{\text{AGN}}}{\beta_{\text{FS}} c} f_{\text{corr}}$$
$$\sim 1 \text{ yr} \left(\frac{H_{\text{AGN}}}{5 \times 10^{16} \text{ cm}} \right) \left(\frac{\beta_{\text{FS}}}{0.1} \right)^{-1} \left(\frac{f_{\text{corr}}}{3} \right). \tag{4}$$

Here $\beta_{\rm FS} \sim (7/6)\beta_{\rm h}$ is the dimensionless velocity of the forward shock of the jet head, and $f_{\rm corr}$ is the correction factor for the delay time due to the inclination of the jet and the geometry of the cavity. Ignoring geometrical corrections due to the existence of the cavity, we assume $f_{\rm corr} = \min[1/\cos i, 1/\theta_0 \sin i]$, considering both the cases in which the shocked gas (cocoon) breaking out of the AGN disk is from its head and from its sides, where i is the angle between the jet and the angular momentum direction of the AGN disk. With this prescription, $f_{\rm corr}$ ranges between ~ 1 and $1/\theta_0$. Note that Equation (3) is valid for $\beta_{\rm h} \leqslant 1$, which can be rewritten as

$$L_{\rm j} \lesssim 3 \times 10^{48} \, {\rm erg \ s^{-1}} \Biggl(\frac{\rho_{\rm AGN}}{10^{-11} \, {\rm g \ cm^{-3}}} \Biggr) \Biggl(\frac{t_{\rm break}}{1 \, {\rm day}} \Biggr)^2 \Biggl(\frac{\theta_0}{0.2} \Biggr)^4.$$
 (5)

This condition is satisfied for all models in this paper (Tables 2 and 3).

After the shock breakout, radiation is produced. Early emission is characterized by the breakout emission as described in Section 2.3 and Paper I, while later emission is characterized by the shock cooling radiation described in Section 2.2. Since breakout emission is associated with the shock propagation, both nonthermal and thermal emissions are expected. On the other hand, we only consider thermal emission from shock cooling and neglect any nonthermal emission from expanding ejecta. The latter can also be bright if additional strong shocks form when the ejecta collide with the interstellar medium. We use the nonthermal component of the breakout emission and the thermal shock cooling emission to model the flares reported by Graham et al. (2023), since these are bright in optical bands. Note that the peak frequency of the thermal breakout emission from the jet head falls above the X-ray bands, which is constrained by the duration of the flare (e.g., Equations (21) and (27) below), and hence it cannot reproduce the optical flares.

2.2. Shock Cooling Emission

2.2.1. Physical Model

In the shock cooling emission, photons diffuse and are released from deep inside the shocked gas, as observed in supernovae (Arnett 1980). To present the properties of this emission, we first describe the evolution of the shocked gas.

At the breakout of the shocked gas at $t = t_{break}$, the thermal energy of the shocked gas is roughly given by

$$e_{\rm BO} = \frac{1}{2} m_{\rm BO} \beta_{\rm c}^2 c^2,$$
 (6)

where

$$\beta_{\rm c} \simeq \beta_{\rm h} \theta_0 \tag{7}$$

is the dimensionless velocity of the shocked gas (Bromberg et al. 2011), and $m_{\rm BO}$ is the mass of the shocked gas at the breakout and is roughly given by

$$m_{\rm BO} \simeq 2\pi H_{\rm AGN}^3 f_{\rm corr}^3 \theta_0^2 \rho_{\rm AGN},$$
 (8)

considering the cylindrical shape of the shocked gas with the height of $H_{AGN}f_{corr}$ and the radius of $H_{AGN}f_{corr}\theta_0$. After the shock passage (even before the shock breakout), the internal energy of the shocked gas is converted to kinetic energy due to the expansion caused by the radiation pressure. Afterward, the shocked ejecta expands nearly spherically with velocity $v_{\rm ei} \sim \beta_{\rm c} c$. Here, the velocity of the shocked gas (Equation (7)) is evaluated by assuming that all the energy carried by the jet is converted into radiation pressure of the shocked gas, and the radiation pressure then acts to accelerate the shocked gas. Note that this analytical expression derived by Bromberg et al. (2011) has been confirmed by numerical simulations (e.g., Mizuta & Ioka 2013). Also note that, while we consider the emission from the shocked AGN gas, we neglect that from the shocked jet (e.g., Matzner 2003; Nakar & Piran 2017; Chen et al. 2023a; Hamidani & Ioka 2023). The latter is uncertain due to the unconstrained fraction of mixing between the jet and the AGN gas, and further studies would be required to understand its observability.

As the ejecta expands to size *R*, the optical depth of the spherically expanding ejecta declines as (e.g., Nakar & Piran 2017; Sapir & Waxman 2017)

$$\tau_{\rm ej} \simeq \frac{\kappa_{\rm ej} m_{\rm BO}}{4\pi R^2},$$
(9)

where $\kappa_{\rm ej}$ is the ejecta's opacity. We adopt the Thomson scattering opacity of $\kappa_{\rm ej} \sim 0.4~{\rm g~cm^{-2}}$ assuming ionized gas. If the ejecta is initially optically thick, as assumed in our fiducial model, photons deep inside the ejecta can be diffused out once the optical depth is reduced to

$$\tau_{\rm ei} = c/v_{\rm ei} \tag{10}$$

at the time

$$t_{\text{diff}} = \left(\frac{\kappa_{\text{ej}} m_{\text{BO}}}{4\pi c v_{\text{ej}}}\right)^{1/2},\tag{11}$$

when the corresponding radius is $R_{\text{diff}} = t_{\text{diff}} v_{\text{ej}}$ and the density

$$\rho_{\text{diff}} = \frac{c}{\kappa_{\text{ej}} R_{\text{diff}} \nu_{\text{ej}}} = \frac{c}{\kappa_{\text{ej}} t_{\text{diff}} \nu_{\text{ej}}^2}.$$
 (12)

Due to the adiabatic expansion, the thermal energy at the diffusion radius is reduced by a factor of $\sim (R_{\rm BO}^3/R_{\rm diff}^3)^{\gamma-1}$, where $\gamma=4/3$ is the adiabatic index for the radiation-pressure-dominated gas, $R_{\rm BO}=(V_{\rm BO}/4\pi)^{1/3}$ is the typical size, and $V_{\rm BO}$ is the volume of the shocked gas at the shock breakout. Hence, the luminosity at $\tau_{\rm ej}=c/v_{\rm ej}$ is related to $e_{\rm BO}$ as

$$L_{\rm SC} = \frac{e_{\rm BO}}{t_{\rm diff}} \frac{R_{\rm BO}}{R_{\rm diff}}.$$
 (13)

Using $R_{\rm BO}$ in Equation (13), the unperturbed AGN density at the position of the BH ($R = R_{\rm BH}$) can be estimated via

$$\rho_{\rm AGN} \sim \rho_{\rm diff} \left(\frac{R_{\rm diff}}{R_{\rm BO}}\right)^3.$$
(14)

Furthermore, from the AGN density, the inflow rate of the AGN disk at $R = R_{\rm BH}$ can be calculated via

$$\dot{M}_{\text{inflow}} = 4\pi H_{\text{AGN}}^3 \rho_{\text{AGN}} \Omega \alpha \tag{15}$$

assuming an alpha viscosity with parameter α , and where Ω is the orbital angular velocity of the BH around the SMBH. Here, the AGN luminosity $(L_{\rm AGN})$ is related to the inflow rate as

$$\frac{L_{\text{AGN}}}{\eta_{\text{rod}}c^2} = \dot{M}_{\text{SMBH}} = f_{\text{cons}}\dot{M}_{\text{inflow}},\tag{16}$$

where $\dot{M}_{\rm SMBH}$ is the accretion rate onto the SMBH, $\eta_{\rm rad}$ is the radiation efficiency, and $f_{\rm cons} \equiv \dot{M}_{\rm SMBH}/\dot{M}_{\rm inflow} \leqslant 1$ is the fraction of the inflow rate at $R=R_{\rm BH}$ over the accretion rate onto the SMBH.

The radiation temperature is determined as follows (see Section 3.4 for discussions). At $\tau_{\rm ej} = c/v_{\rm ej}$, the energy density of the radiation within the ejecta shell is

$$u_{\gamma} = \frac{L_{\text{SC}} \tau_{\text{ej}}}{4\pi R_{\text{diff}}^2 c}.$$
 (17)

The blackbody temperature of the radiation is then given by

$$T_{\rm BB} = (u_{\gamma}/a)^{1/4},$$
 (18)

where a is the radiation constant. Note that the radiation pressure dominates the gas pressure at $t \lesssim t_{\rm diff}$ for the models considered in this paper. Since the flares in Graham et al. (2023) were found by the Zwicky Transient Facility (ZTF), and the observed optical luminosity ($L_{\rm obs}$) can be roughly estimated as the total observed energy of the flare in the optical band divided by the duration (provided in Table 3 of Graham et al. 2023), we pose that $L_{\rm obs}$ needs to match the luminosity in the ZTF bands as

$$L_{\text{obs}} = L_{\text{SC}} \int_{\nu_{\text{down}}}^{\nu_{\text{up}}} \frac{2h\nu^3}{c^2} \frac{d\nu}{e^{h\nu/k_{\text{B}}T_{\text{BB}}} - 1} / \sigma T_{\text{BB}}^4, \tag{19}$$

where $\nu_{\rm up} = c/(400 \, {\rm nm})$ and $\nu_{\rm down} = c/(700 \, {\rm nm})$ are the upper and lower limits for the frequencies observed by the r and g bands of the ZTF. Note that the luminosities in the r and g bands of the ZTF are not directly derived from Equation (19). To calculate them (panels (c) and (d) of Figure 3), we adjust the limits of the integral in this equation to cover the frequency range of the relevant band.

2.2.2. Derivation of Model Parameters

Using Equations (1)–(19), we can then determine the 17 quantities $\beta_{\rm c}$, $\rho_{\rm AGN}$, $R_{\rm BH}$, $H_{\rm AGN}$, $L_{\rm j}$, $\dot{m}_{\rm BHL}$, $t_{\rm break}$, $e_{\rm BO}$, $m_{\rm BO}$, $\tau_{\rm ej}$, $\rho_{\rm diff}$, $R_{\rm BO}$, $R_{\rm diff}$, u_{γ} , $T_{\rm BB}$, $L_{\rm SC}$, and $\dot{M}_{\rm inflow}$ given the input parameters, $\theta_{\rm O}$, $f_{\rm acc}$, $a_{\rm BH}$, α , $\eta_{\rm rad}$, $f_{\rm corr}$, and $f_{\rm cons}$, and the observed properties, $L_{\rm obs}$, $L_{\rm AGN}$, and $t_{\rm diff}$. For example, combining Equations (1)–(16), the velocity of the shocked gas is calculated as

$$\beta_{\rm c} = \left[\frac{32\pi^4 f_{\rm jet/BHL}^3 f_{\rm cons} A c^{10} G^2 m_{\rm BH}^2 t_{\rm diff}^2 \alpha \eta_{\rm rad}}{9L_{\rm AGN} L_{\rm SC}^3 \kappa_{\rm ej}^4 f_{\rm corr}^6} \right]^{\delta}, \qquad (20)$$

where $f_{\rm jet/BHL} \equiv f_{\rm f} f_{\rm acc} \eta_{\rm j}$ is a parameter related to the jet power, and A and δ are variables depending on the velocity of the shocked gas. For $\beta_{\rm c}/\theta_0 < 1$, $A = (35/18)^6 \theta_0^{-3}$ and $\delta = 1/2$, and otherwise (as long as the jet is in the collimated regime), $A = \theta_0$ and $\delta = 1/8$. To determine $\beta_{\rm c}$ using Equation (20), $L_{\rm SC}$ needs to be derived using Equations (17)–(19). To consistently solve these equations, we calculate $\beta_{\rm c}$ in an iterative way using Newton's method. Then, by incorporating $\beta_{\rm c}$ into Equations (1)–(19), the other parameters can also be determined.

We further adjust $f_{\rm jet/BHL}$ so that the scale height of the AGN disk is equal to the height expected for the Shakura–Sunyaev disk, given α . Such disk structure is expected to be realized in regimes where the Toomre parameter (Equation (22)) becomes greater than 1.

2.3. Breakout Emission

2.3.1. Physical Model

Long before photons deep inside the ejecta escape $(t \sim t_{\rm break} + t_{\rm diff})$, at around the time that the shock arrives at the surface of the ejecta $(t \sim t_{\rm break})$, bright breakout emission is released. Since breakout emission of the jet head is associated with the shock propagation, both nonthermal and thermal emission are expected. Such nonthermal emission can explain the optical flares found by Graham et al. (2020), as investigated in Paper I. In the following, we describe how to reconstruct the model properties for the breakout emission.

Photons inside the shock start to diffuse out from the AGN disk and the breakout emission begins to be released when the photon diffusion time from the shock front, $t_{\rm diff,sh} \sim d_{\rm edge}^2 \kappa_{\rm sh} \rho_{\rm AGN}/c$, becomes equal to the dynamical timescale of the shock, $t_{\rm dyn,edge} \sim d_{\rm edge}/\beta_{\rm FS}c$, where $d_{\rm edge}$ is the thickness of the AGN disk above the shock, and $\kappa_{\rm sh}$ is the opacity of the shocked gas. By equating these timescales, the thickness at the breakout is given by $d_{\rm edge,BO} \sim 1/(\beta_{\rm FS}\kappa_{\rm sh}\rho_{\rm AGN})$, and the duration of the emission from a breakout shell is

$$t_{\text{diff,BO}} \sim 1/(\beta_{\text{FS}}^2 c \kappa_{\text{sh}} \rho_{\text{AGN}})$$

 $\sim 3 \text{ yr} \left(\frac{\beta_{\text{FS}}}{0.1}\right)^{-2} \left(\frac{\rho_{\text{AGN}}}{1 \times 10^{-16} \text{ g cm}^{-3}}\right)^{-1},$ (21)

where we adopt $\kappa_{\rm sh} \sim 0.4 \, {\rm g \ cm}^{-2}$ considering the ionization of gas by photons released from the shocks (Nakar & Sari 2010).

If we assume that the AGN disk is gravitationally unstable at the position of the BH, which is expected for the delay time and the duration of the flares (Paper I), the density of the AGN disk is related to the position of the BH through (e.g., Thompson et al. 2005)

$$\frac{\Omega^2}{\sqrt{2}\pi G\rho_{\text{AGN}}} = Q \simeq 1, \tag{22}$$

where Q is the Toomre parameter. Note that AGN disks at the BH positions are predicted to be Toomre unstable (Table 2; e.g., Haiman et al. 2009).

2.3.2. Derivation of Model Parameters

Using Equations (1)–(4) and (21)–(22), we can determine the six variables β_h , ρ_{AGN} , R_{BH} , H_{AGN} , L_j , and \dot{m}_{BHL} , given θ_0 , f_{acc} , and η_j . For example, the velocity of the jet head is calculated by

$$\beta_{\rm h} = \left[\frac{5(7/6)^{4/3} f_{\rm jet/BHL} m_{\rm BH}^{2/3} G^{1/2} \left(\frac{c \kappa_{\rm sh} t_{\rm diff,BO}}{\sqrt{2} \pi} \right)^{1/6}}{3^{5/3} f_{\rm corr} t_{\rm break} \theta_0^4 c^2} \right]^{3/11}.$$
(23)

Then, by incorporating β_h into Equations (1)–(4) and (21)–(22), the other parameters can also be determined.

In the case of breakout emission, $R_{\rm BH}$ is found to be large (Section 3.2). At such large scales, efficient transfer of angular momentum of the AGN gas is required for SMBH accretion (Thompson et al. 2005). Following Thompson et al. (2005), we assume that the inflow rate of the AGN disk is parameterized by

$$\dot{M}_{\rm inflow} = 4\pi R_{\rm BH} H_{\rm AGN}^2 \rho_{\rm AGN} \Omega m. \tag{24}$$

2.4. Evolution

In this section, we describe the evolution of the luminosity and temperature for thermal emission from the shocked gas in the breakout and shock cooling emission phases. Referring to previous studies (Arnett 1980; Nakar & Sari 2010; Piro et al. 2021; Morag et al. 2023), we assume that the luminosity

evolves as

$$L(t') \sim \frac{e_{BO}}{t_{\text{dyn}}} \begin{cases} 0 & \text{for } t' \lesssim 0, \\ 1 & \text{for } 0 \lesssim t' \leqslant t_{\text{pl}}, \\ \left(\frac{t'}{t_{\text{pl}}}\right)^{-4/3} & \text{for } t_{\text{pl}} \leqslant t' \lesssim t_{\text{sph}}, \\ \left(\frac{t_{\text{sph}}}{t_{\text{pl}}}\right)^{-4/3} \left(\frac{t'}{t_{\text{sph}}}\right)^{-\frac{2.28n-2}{3(1.19n+1)}} & \text{(25)} \\ & \text{for } t_{\text{sph}} \leqslant t' \leqslant t_{\text{diff}}, \\ \left(\frac{t_{\text{dyn}}}{t_{\text{diff}}} \frac{R_{BO}}{R_{\text{diff}}} \exp \left[-\frac{1}{2} \left(\frac{t'^2}{t_{\text{diff}}^2} - 1\right)\right] & \text{for } t_{\text{diff}} \leqslant t', \end{cases}$$

where $t'=t-t_{\rm break}$, $t_{\rm pl}=1/(\beta_{\rm c}^2c\kappa_{\rm ej}\rho_{\rm AGN})$ is the duration of emission from a breakout shell in the shocked gas, $t_{\rm sph}\simeq R_{\rm BO}/\beta_{\rm c}c$ is the transition between the planar and spherical geometries of the breakout shell, $t_{\rm dyn}=H_{\rm AGN}/\beta_{\rm c}c$ is the dynamical timescale, and n is the power-law slope of the vertical AGN gas density profile at the height at which photons begin to break out. The second and third rows correspond to the luminosity in the planar phase (before the shocked gas doubles its radius by expansion) for the breakout emission, the fourth row corresponds to that in a spherical phase (after the shocked gas doubles and before the shock cooling emission phase), and the fifth row corresponds to that in a shock cooling emission phase.

Similarly following previous studies, we assume that the temperature evolves as

Inherature evolves as
$$\begin{cases}
1 & \text{for } 0 \lesssim t' \leqslant t_{\text{pl}}, \\
\left(\frac{t'}{t_{\text{pl}}}\right)^{-\frac{2}{3}\frac{9n+5}{317n+9}} & \text{for } t_{\text{pl}} \leqslant t' \lesssim t_{\text{sph}}, \\
\left(\frac{t_{\text{sph}}}{t_{\text{pl}}}\right)^{-\frac{2}{3}\frac{9n+5}{317n+9}} \left(\frac{t'}{t_{\text{sph}}}\right)^{n_{\text{T}}} & \text{(26)} \\
& \text{for } t_{\text{sph}} \leqslant t' \leqslant t_{\text{diff}}, \\
\frac{T_{\text{BB}}}{T_{\text{BB},0}} \left(\frac{t'^2}{t_{\text{diff}}^2} - 1\right)^{-1/2} & \text{for } t_{\text{diff}} \leqslant t',
\end{cases}$$

where

$$T_{\rm BB,0} = (7\rho_{\rm AGN}\beta_{\rm c}^2 c^2/2a)^{1/4} \tag{27}$$

is the blackbody temperature of the breakout shell, $n_{\rm T}$ is the power-law index for the temperature evolution in the spherical phase, and $n_{\rm T} = -(18.48n^2 + 20.69n + 6)/[(1.19n + 1)(22.32n + 17)]$ for an expanding spherical ejecta (Nakar & Sari 2010). The validity of these analytical formulae has been tested by recent numerical simulations (e.g., Piro et al. 2021; Morag et al. 2023).

Since Equations (25) and (26) are formulae for an expanding ejecta with a spherically symmetric evolution, some modifications are required in the cases of emission from an expanding ejecta with a cylindrical shape like a cocoon (shocked gas), especially at around the transition between the planar and spherical phases. For simplicity, we determine n and n_T so that the luminosity and the temperature smoothly evolve at $t' = t_{\text{diff}}$, respectively.

2.5. Parameters

In this section, we describe the fiducial values for the model parameters and the observed properties of the flares used in the modelings.

As fiducial values, we set the opening angle of the injected jet to $\theta_0 = 0.2$ (e.g., Hada et al. 2013; Berger 2014; Hada et al. 2018), the radiation efficiency to $\eta_{\rm rad} = 0.1$, the correction factor for the delay time to $f_{corr} = 3$ (which roughly corresponds to the median value considering the cavity with the aspect ratio of ~ 1 and isotropic jet directions), the consumption fraction of the inflow rate to $f_{cons} = 1$, the alpha-viscous parameter to $\alpha = 0.1$, and the angular momentum transfer parameter in the outer regions of the AGN disk to m = 0.1. For the computation of the shock cooling emission, we adjust the value of $f_{\text{jet/BHL}} \equiv f_c f_{\text{acc}} \eta_i$ so that the scale height of the AGN disk is equal to the height expected for the Shakura-Sunyaev disk (Section 2.2), while for the breakout emission, we set it to $f_{\text{jet/BHL}} = 10$ assuming $f_{\text{c}} = 10$ (Tanigawa & Watanabe 2002), $\eta_{\rm j} = 0.5$, and $f_{\rm acc} = 2$ considering moderate enhancement of accretion due to shocks caused by recoil kicks (Appendix B of Tagawa et al. 2023b).

When modeling the flares with breakout emission, we assume that the flare duration (t_{duration}) corresponds to the exponential decay time (t_e) in Graham et al. (2023). To derive the delay time $(t_{\rm delay})$, we identify the day on which the flare luminosity peaks using digitizer. Due to the difficulty of identifying the peak, $t_{\rm delay}$ contains uncertainties. We adopt $M_{\rm SMBH}$ and $m_{\rm BH}$ from Tables 3 and 4 of Graham et al. (2023). The optical luminosity is derived by means of the total observed energy in the optical band divided by the sum of the rise time (t_{ϱ}) and the decay time (t_e) presented in Graham et al. (2023). We calculate the luminosity of the AGNs (L_{AGN}) by inferring the flux of the AGNs at \sim 4000 Å from Figure 6 of Graham et al. (2023) and estimating the luminosity distance from the redshift of the GW events assuming a value for the Hubble constant of $67.8\,\mathrm{km\,s^{-1}\,Mpc^{-1}}$ for the matter density today of 0.24 and for the cosmological constant today of 0.74 (Planck Collaboration et al. 2016) and adopting a bolometric correction factor of 5 (Duras et al. 2020). The values for the observed quantities adopted in this paper are listed in Table 1. Note that the delay time (t_{delay}) corresponds to t_{break} , and the duration of a flare (t_{duration}) corresponds to $t_{\text{diff,BO}}$.

Conversely, when modeling the flares with shock cooling emission, we assume that the duration of a flare $(t_{\rm duration})$ corresponds to $t_{\rm diff}$. The delay time between a GW event and an optical flare $(t_{\rm delay})$ is also on the order of $\sim t_{\rm diff}$ given $t_{\rm break} \ll t_{\rm diff}$, while we do not use the delay time $(t_{\rm delay})$ to constrain the model parameters. Note that the $t_{\rm delay} \sim t_{\rm duration}$ expected in this scenario is roughly consistent with the properties of the observed flares (Table 1). We assume that the observed optical luminosity of the flare $(L_{\rm op})$ corresponds to the luminosity in the ZTF bands $(L_{\rm ops})$.

We note that in our model, the physical properties are uniquely determined. This is because we fixed several input parameters as detailed above, and we do not directly use the observational data points for parameter fitting. If instead we allowed the input parameters to vary, we would introduce degeneracies among several input parameters. The variations of the values of the fixed input parameters can affect the physical properties of the model, especially in the breakout emission

https://automeris.io/WebPlotDigitizer/

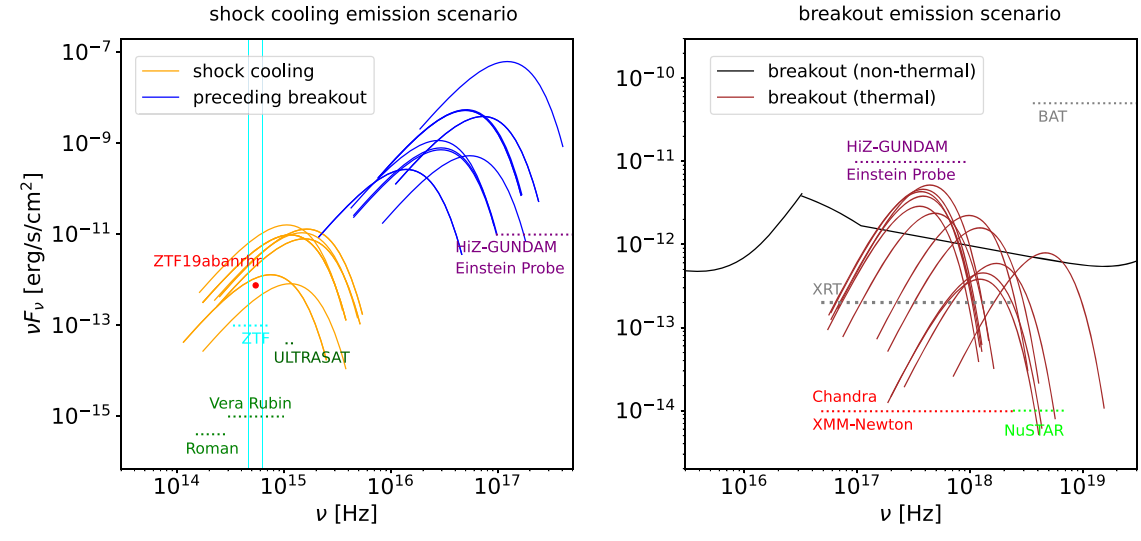


Figure 2. The SEDs for shock cooling (orange) and preceding breakout emission (blue) from shocked gas in the shock cooling emission scenario for pairs 1–12 (left panel) and those for thermal breakout emission (brown) from a jet head in the breakout emission scenario (right panel) assuming a luminosity distance of $d_L = 3$ Gpc. The SEDs for the nonthermal emission are drawn for the model adopted in Figure 5 of Paper I as a representative example. The dotted blue, purple, red, light green, dark green, and gray lines mark the sensitivity of ZTF, HiZ-GUNDAM and Einstein Probe, Chandra and XMM-Newton, NuSTAR, ULTRASAT, the Vera Rubin Observatory, and Roman Space Telescope, and Swift BAT, respectively, as adopted in Paper I. The vertical cyan lines present the g and r bands of ZTF. Note that the shock cooling emission is too dim ($\ll 10^{-17}$ erg s⁻¹ cm⁻²) in the breakout emission scenario to be visible in the right panel.

scenario, while affecting them less in the shock cooling emission scenario (see Sections 4.1 and 4.2). We believe that such simple prescriptions are useful to understand the typical properties expected from the model and consider possible tests of the model below.

3. Results and Discussions

3.1. Shock Cooling Emission

Table 1 shows the list of possible pairs of associations between the GW events and the electromagnetic flares reported in Graham et al. (2023), along with their observed properties. Seven electromagnetic flares and 12 pairs for the possible associations are reported. The number of pairs (12) is larger than that of the flares (7), because some flares can be associated with more than one GW event. Hence, at least five pairs are false associations. Note that in this paper we do not analyze the two gamma-ray flares possibly associated with GW events due to their significantly different properties (Bagoly et al. 2016; Connaughton et al. 2016), while they can be explained by the thermal breakout emission from the jet head in relativistic regimes (Tagawa et al. 2023b).

Table 2 shows the distribution of the model parameters when the properties of the observed flares (Table 1) are modeled with shock cooling emission.

The parameter $f_{\rm jet/BHL}$ is widely distributed depending on the pairs. $f_{\rm jet/BHL} \sim 1$ –10 in pairs 4, 11, and 12 is roughly expected for the Bondi–Hoyle–Lyttleton accretion, while $f_{\rm jet/BHL} \sim 10$ –60 in pairs 1–3, 5, and 7–10 can be realized by the enhancement of accretion by shocks due to recoil kicks at merger (Paper I). However, $f_{\rm jet/BHL} \sim 3000$ in pair 6 is difficult to realize, since only up to $f_{\rm jet/BHL} \lesssim 300$ is found to be feasible by considering the radial surface density profile of a circum-BH disk and appealing to the results of numerical simulations (see Appendix B of Paper I). On the other hand, even for pair 6, if we adopt $f_{\rm corr} \sim 1$, $f_{\rm jet/BHL}$ is reduced to ~ 300 . This is presumably because both a high accretion rate and a low inclination have similar influences on the breakout velocity, and most parameters are mainly characterized by the magnitude

of the breakout velocity. Due to the variation of $f_{\rm corr}$ (between ~ 1 and $1/\theta_0$) and the degeneracy between $f_{\rm corr}$ and $f_{\rm jet/BHL}$, the cooling model is poorly constrained or tested by the value of $f_{\rm jet/BHL}$.

The parameter $R_{\rm BH}$ ranges between 0.06 and 0.3 pc, corresponding to 900–6 × 10⁴ R_g , where $R_{\rm g} = GM_{\rm SMBH}/c^2$ is the gravitational radius of the SMBH. These locations roughly correspond to migration traps, gap-forming regions, and/or slow migration regions, where BH mergers are predicted to be frequent (Bellovary et al. 2016; Tagawa et al. 2020b).

The orange lines in the left panel of Figure 2 show the spectral energy distributions (SEDs) for pairs 1-12. The radiation temperature ranges between $T_{\rm BB} = 9200$ and 20,000 K, corresponding to the peak wavelength $\lambda_{\text{peak}} = ch/(3k_{\text{B}}T_{\text{BB}}) =$ $240-520 \,\mathrm{nm}$, where h is the Planck constant and k_{B} is the Boltzmann constant. Also, the various colors observed in the optical flares (Figure 3 of Graham et al. 2023) can be reproduced depending on the variation of the radiation temperature with changing some input parameters, such as the direction of the jet (i). For example, if we set $i = 0^{\circ}$ (the jet being perpendicular to the AGN disk plane) by using derived values for ρ_{AGN} , R_{BH} , and H_{AGN} and the observed parameters (m_{BH} and M_{SMBH}), the radiation temperature of the flares is enhanced by a factor of \sim 1.7. This is because for $i = 0^{\circ}$, the shocked mass becomes low, and then photons can escape from an earlier phase when the radiation temperature is higher. Thus, the variety of colors can be reproduced if there are temperature variations in the thermal emission. For synchrotron emission (whose possible contribution to the flares is discussed in Section 3.2), the color is related to the power-law slope of the injected electrons accelerated by the first-order Fermi process (p) as $\nu L_{\nu} \propto \nu^{(-p+2)/2}$, and p is presumably distributed in a narrow range for the same phenomena (Panaitescu & Kumar 2001). On the other hand, various values for the color can be realized if the breaks of the power laws in the SEDs coincidentally fall at around the ZTF bands (see the black line in the right panel of Figure 2). Note that the distribution of the colors is currently uncertain due to the shift in the baseline of the flux and the contribution from the background AGN emission in

Figure 3 of Graham et al. (2023). If the color is actually distributed in a wide range, the flares are then easier to model by thermal shock cooling emission rather than by nonthermal breakout emission. In addition, the model can be also discriminated by constraining the spectral shape of the emission. This can be done by simultaneously observing the flares with the ZTF, the Vera Rubin Observatory (Ivezić et al. 2019), the Roman Space Telescope (Spergel et al. 2015), and the Ultraviolet Transient Astronomy Satellite (ULTRASAT; Shvartzvald et al. 2024; Figure 2) in the future.

We also predict breakout emission from the shocked gas preceding the shock cooling emission (this is the emission from the shocked gas, which is different from the emission from the jet head discussed in Section 3.2). The duration of the breakout emission from the shocked gas,

$$t_{\text{diff,CBO}} = \frac{1}{\beta_c^2 c \kappa_{\text{ej}} \rho_{\text{AGN}}},$$
 (28)

is distributed in the range $t_{\rm diff,CBO} \sim 10{\text -}10^5 \, {\rm s}$ (the rightmost column of Table 2), and the temperature (Equation (27)) is in the range $2 \times 10^5{\text -}2 \times 10^6 \, {\rm K}$ (blue lines in the left panel of Figure 2). Although the duration of the breakout emission is shorter than than that of the shock cooling emission, it could be detected by future X-ray surveys, such as HiZ-GUNDAM (Yonetoku et al. 2020) and/or the Einstein Probe (Yuan & Narayan 2014).

Figures 3(a) and (b) show the evolution of the luminosity and the temperature of emission for pairs 1, 5, and 11. We chose pair 1 as a fiducial example, pair 5 as an event with small $m_{\rm BH}$, and pair 11 as the one with long $t_{\rm duration}$. The lines are drawn until the phase at which $\tau_{\rm ej}=1$ is satisfied, since our model for thermal emission is not valid when $\tau_{\rm ej}<1$. In panel (b) we also indicate, by drawing a line, the region below which the evolution of the properties predicted by our model becomes inaccurate due to the fact that recombination becomes effective (e.g., Morag et al. 2023).

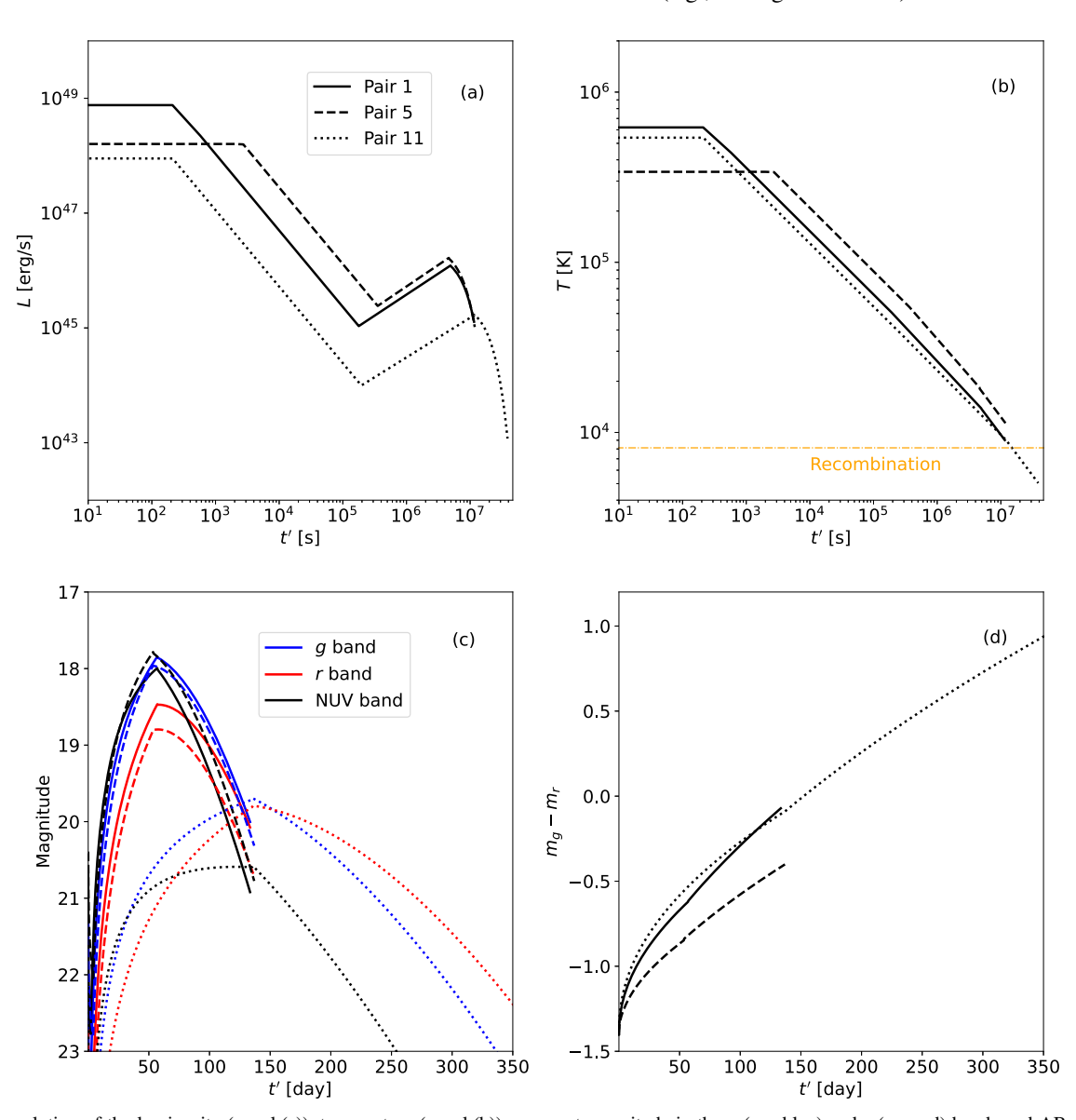


Figure 3. The evolution of the luminosity (panel (a)), temperature (panel (b)), apparent magnitude in the g (m_g , blue) and r (m_r , red) bands and AB magnitude at a near-ultraviolet band (260 nm, black; panel (c)), and the color ($m_g - m_r$, panel (d)) for thermal emission in the shock cooling emission model for pairs 1 (solid), 5 (dashed), and 11 (dotted). We present pairs 1, 5, and 11 as a fiducial, a smaller $m_{\rm BH}$, and a longer $t_{\rm duration}$ case, respectively, among which evolution timescales are derived to be different. Lines are drawn until $\tau_{\rm ej} = 1$, after which our model is invalid. In panel (b), the temperature below which recombination becomes effective and the lightcurve becomes inaccurate (e.g., Morag et al. 2023) is indicated with an orange dotted–dashed line.

For the smaller $m_{\rm BH}$ case (dashed lines in Figure 3), the timescale for the breakout emission of the shocked gas $(t_{\rm pl})$ is longer. This is because $L_{\rm j}$ is lower due to the lower Bondi–Hoyle–Lyttleton rate (Equations (1) and (2)), and $\beta_{\rm c}$ tends to be lower for lower $L_{\rm j}$ (Equations (3) and (20)). To reproduce $t_{\rm diff}$, $\rho_{\rm AGN}$ needs to be lower for lower $\beta_{\rm c}$ (Equation (11)). Due to the low $\beta_{\rm c}$ and $\rho_{\rm AGN}$ (Table 2), the breakout timescale of the shocked gas $(t_{\rm pl} \propto \beta_{\rm c}^{-2} \rho_{\rm AGN}^{-1})$ becomes longer. In such a case, since photons diffuse out from the shocked gas earlier, adiabatic expansion is inefficient, leading to a higher temperature.

For the longer t_{duration} model (dotted lines in Figure 3), the evolution of the luminosity is slower in the shock cooling regime ($t' \gtrsim t_{\text{diff}}$).

3.2. Breakout Emission

Table 3 shows the parameters of the breakout emission model reproducing the properties of the observed flares. In this model, the parameters are distributed in narrow ranges. The mergers are predicted to occur at $R_{\rm BH} \sim 1$ –10 pc, the shock velocity ranges within $\beta_{\rm h} \sim 0.3$ –0.4, the disk aspect ratio at $R_{\rm BH}$ ranges within $h_{\rm AGN} \equiv H_{\rm AGN}/R_{\rm BH} \sim 0.001$ –0.02, the fraction of the optical luminosity to the kinematic power of the shock is around $L_{\rm op}/L_{\rm j} \sim 0.02$ –1, the fraction of the distance from the SMBH to the size of the nuclear star cluster ($R_{\rm NSC}$) ranges within $R_{\rm BH}/R_{\rm NSC} \sim 0.2$ –0.7 assuming the empirical relation of $R_{\rm NSC} = 8.3~{\rm pc}(M_{\rm SMBH}/3.1 \times 10^8~M_{\odot})^{0.154}$ (Kormendy & Hox 2013; Scott & Graham 2013; Georgiev et al. 2016), and the inflow rate of an AGN disk in units of the Eddington rate varies within $\dot{M}_{\rm inflow}/\dot{M}_{\rm Edd} \sim 0.004 - 1.2$, where $\dot{M}_{\rm Edd} \equiv L_{\rm Edd}/c^2\eta_{\rm rad}$ with a radiative efficiency of $\eta_{\rm rad} = 0.1~{\rm and}~L_{\rm Edd}$ is the Eddington luminosity of the SMBH.

We find that the optical luminosity of the flare is lower than the kinetic power of the jet $(f_{\rm op/kin} < 1)$ for all the pairs (Table 3). Considering the bolometric correction of the breakout emission in the optical band (\sim 10; Paper I), our scenario demands $f_{\rm op/kin} \lesssim 0.1$. For the pairs that do not satisfy this condition, we need to use $f_{\rm jet/BHL} > 10$. Note that a higher value ($f_{\rm jet/BHL} \lesssim 100$) is possible by considering the enhancement of the accretion rate due to shocks caused by recoil kicks at merger (Appendix B of Paper I).

In the right panel of Figure 2, the SEDs for thermal emission from the breakout of the jet head for pairs 1–12 are displayed. As they are bright at $\sim \! 10^{17} \! - \! 10^{19} \, \text{Hz}$ and the duration is long $(\gtrsim \! 10^6 \, \text{s})$, they can be observed by X-ray telescopes, such as the Swift X-ray Telescope (Burrows et al. 2005), Chandra, XMM-Newton (Jansen et al. 2001), and the Nuclear Spectroscopic Telescope Array (NuSTAR; Harrison et al. 2013). Note that the shock cooling emission associated with the breakout emission in all the pairs is so dim ($\ll \! 10^{40} \, \text{erg s}^{-1}$) that it is buried within the AGN variability.

The derived values of $R_{\rm BH}/R_{\rm NSC} \sim 0.2-0.7 \sim 1-8$ pc are much larger than in the shock cooling case. The different locations are driven by the phases of the emission. In our model, the duration of the flares corresponds to the timescale at which the diffusion timescale is equal to the dynamical timescale (e.g., Equations (12) and (21) for the shock cooling and breakout emission cases, respectively). This timescale is inversely proportional to the density of the ejecta or the AGN disk, as well as to the square of the velocity of the ejecta or the shocks in the shock cooling and breakout emission scenarios, respectively. As a result, since the velocities are typically

comparable (Tables 2 and 3), the density of the AGN disk in the breakout emission scenario must be similar to the density of the ejecta in the shock cooling emission scenario in order to reproduce the duration of the flares. Additionally, in the shock cooling emission scenario, the density of the ejecta is much lower than the local AGN density due to adiabatic expansion (Equation (14)). Thus, the AGN density is typically much lower in the breakout emission scenario; therefore, the distance from the SMBH needs to be larger. These larger distances are consistent with the scenario that BHs in nuclear star clusters are captured by AGN disks and merge with one another. Here, the migration timescale of objects in AGN disks around massive SMBHs as inferred for the flaring AGNs (Table 1) is so long that migration before BH mergers is less expected.

To check whether the values derived for the aspect ratio $(h_{\rm AGN})$ are plausible, we calculate the aspect ratio of the AGN disk $(h_{\rm AGN,TQM})$ adopting the model in Thompson et al. (2005), using $R_{\rm BH}$, $M_{\rm SMBH}$, $M_{\rm inflow}$, and m. We find that the values of $h_{\rm AGN,TQM}$ are roughly comparable to $h_{\rm AGN}$ within a factor of \sim 2 (ninth column of Table 3). Such moderate differences could arise due to the variation of $f_{\rm corr}$ reflecting the variation of the inclination of the jets. In Table 3, we list $f_{\rm corr}$ at which $h_{\rm AGN,TQM} = h_{\rm AGN}$. This shows that $h_{\rm AGN,TQM} = h_{\rm AGN}$ is satisfied by reasonable values for $f_{\rm corr}$ around \sim 3–5.

By comparing $L_{\text{AGN}}/L_{\text{Edd}}$ in Table 1 and $\dot{M}_{\text{inflow}}/\dot{M}_{\text{Edd}}$ in Table 3, we can determine the value of m at which $L_{\rm AGN}/L_{\rm Edd} = \dot{M}_{\rm inflow}/\dot{M}_{\rm Edd}$ as $\dot{M}_{\rm inflow} \propto m$. For pairs 11 and 12, $m \ge 3$ is required to satisfy $L_{AGN}/L_{Edd} \le \dot{M}_{inflow}/\dot{M}_{Edd}$. In the other pairs (1-10), m can be as low as $\ge 0.003-0.5$ to satisfy this condition. We presume that $m \lesssim 1$ is acceptable (e.g., Hopkins & Quataert 2010; Begelman & Armitage 2023; Begelman & Silk 2023), although there are no studies constraining the possible ranges of m as far as we know. Note that the inflow rate at parsec scales can be much higher than the accretion rate onto the central SMBH (e.g., Izumi et al. 2023), since a large fraction of gas is possibly consumed by star formation and outflows, as predicted in Blandford & Begelman (1999), Thompson et al. (2005), and Collin & Zahn (2008). Then $\dot{M}_{\rm inflow}/\dot{M}_{\rm Edd}$ is allowed to be much larger than $L_{\rm AGN}/L_{\rm Edd}$, and the required value of m is enhanced. Hence, pairs 11 and 12 are not well explained by breakout emission due to the required high values of m. On the other hand, it is not clear whether AGN disks are usually in steady state, which might complicate the comparison between the inflow rate and the AGN luminosity.

3.3. Growth of Stellar-mass BHs Implied by Bright Flares

In the following, we examine whether BHs are able to merge before they grow significantly in mass. This is an important issue because highly super-Eddington jet luminosities, and accordingly high accretion rates, are required to explain the properties of the observed flares. For pair 1 in the shock cooling emission scenario, the growth timescale of the BH is as short as $\sim\!50~{\rm yr}(m_{\rm BH}/100~M_\odot)(f_{\rm acc}/15)(L_{\rm j}/10^{48}~{\rm erg~s})^{-1}$, assuming that the accretion rate is enhanced by a factor of $f_{\rm acc}=15$ (Tagawa et al. 2023b) only after mergers. Since the BH typically spends several Myr within an AGN disk before undergoing a merger (Tagawa et al. 2020b), the growth timescale needs to be as high as $\gtrsim\!10~{\rm Myr}$ to avoid significant growth of the BHs in mass.

One possibility to enhance the growth timescale by several orders of magnitude is a low duty cycle for the accretion phases. This is expected due to the formation of a cavity created by the jet launched from the BH. We analyze this effect

following T22 (see their Sections 3.4–3.6), using the parameters listed in Tables 1, 2, and 3, by assuming $\eta_i = 0.1$ and $f_{acc} = 0.3$ (T22) and setting the BH mass to be the mass of the primary BH before merger (85 M_{\odot} for pair 1). With these, the growth timescales for the shock cooling emission and the breakout emission scenarios for pairs 1–12 are estimated to be 3, 3, 1, 1, 1, 1, 2, 2, 3, 3) \times 10⁴ yr, respectively. Note that the duty cycle is much shorter for the shock cooling emission scenario compared to those for the breakout emission scenario. This is because in the shock cooling emission scenario, due to the shorter distance from the SMBH, the (Bondi-like) gas capture rate by the stellar-mass BH is low, and accordingly, the density and ram pressure of the circumbinary disk are low. In addition, due to the short breakout timescale, the velocity and ram pressure of the cocoon are high. These enhance the ejection of circumbinary disks and shorten the duty cycle. In any case, these timescales are still not long enough to sufficiently suppress the growth. Furthermore, such a low duty cycle would reduce the probability for mergers to accompany electromagnetic flares, since BHs need to be active at the time of the mergers for the association between the flares with the GWs. Finally, jets and flares are not produced efficiently by gas capture due to entering fresh AGN gas by GW recoil kicks (Graham et al. 2020), since the angular momentum of the captured gas is so low in our cases (Ruffert & Anzer 1995) that the gas directly accretes onto the BH. Hence, this low duty cycle is unlikely to explain either the bright flares or the growth problem.

An alternative scenario involves amplifying the accretion rate associated with mergers. The sustainability of super-Eddington accretion over an extended period remains an unresolved question, with uncertainties surrounding whether accretion is capped near the Eddington rate due to factors such as wind mass loss, as in the adiabatic inflow-outflow solutions (ADIOS; Blandford & Begelman 1999). By analyzing tidal disruption events and X-ray binaries, Begelman & Volonteri (2017) suggested that the accretion process is significantly modified by whether the radius at which gas circularizes (r_{circ}) is larger than the (spherical) photon trapping radius (r_{trap}). When $r_{\text{circ}} > r_{\text{trap}}$, winds or outflows are launched from wide ranges of radii and solid angles within r_{trap} , and the accretion rate is capped at around the Eddington accretion rate as in the ADIOS. On the other hand, when $r_{\rm circ} < r_{\rm trap}$, the winds can escape from the BH only through narrow ranges of radii and solid angles due to the existence of a weakly bound envelope, which is called a zero-Bernoulli accretion (ZEBRA) flow (Coughlin & Begelman 2014). Then, the mass loss becomes weak, and a super-Eddington accretion is realized.

In our model, circum-BH disks before and after mergers correspond to the former and the latter cases, respectively. Before mergers, $r_{\rm circ}$ is estimated to be $\sim r_{\rm Hill} f_{\rm circ} \sim 8 \times 10^{14} \, {\rm cm} (R_{\rm BH}/0.1 \, {\rm pc}) \, [(m_{\rm BH}/M_{\rm SMBH})/10^{-6}]^{1/3} (f_{\rm circ}/0.4),$ where $r_{\rm Hill}$ is the Hill radius and $f_{\rm circ}$ is a factor estimated to be $\sim\!0.1$ –0.4 (e.g., Tanigawa et al. 2012). Also, $r_{\rm trap} \sim 10^{14} \, {\rm cm} \, [(L_{\rm j}/\eta_{\rm j}f_{\rm jet/BHL})/3 \times 10^{46} \, {\rm erg \, s^{-1}}]$ assuming that the inflow rate at $\sim\! r_{\rm trap}$ is enhanced after mergers by a factor of $f_{\rm jet/BHL}$ due to shocks produced by GW recoil kicks (Tagawa et al. 2023b). Hence, $r_{\rm circ} > r_{\rm trap}$ is satisfied, and the accretion rate is significantly reduced in the ADIOS state as far as $L_{\rm j}/(\eta_{\rm j}f_{\rm jet/BHL}) \lesssim 2 \times 10^{47} {\rm erg \, s^{-1}} (r_{\rm circ}/8 \times 10^{14} \, {\rm cm})$.

On the other hand, after mergers, angular momentum transfer efficiently occurs in circum-BH disks at $\gtrsim r_b \sim 10^{13} \, \mathrm{cm} \, (m_{\mathrm{BH}}/100 \, M_{\odot}) (v_{\mathrm{kick}}/300 \, \mathrm{km \, s^{-1}})^{-2}$ from the BH due to shocks produced by GW recoil kicks, where $r_b \equiv G m_{\mathrm{BH}}/v_{\mathrm{kick}}^2$ and v_{kick} is the recoil kick velocity due to GW radiation. Then, the shocked gas is circularized at $\lesssim r_b$ (Rossi et al. 2010). Thus, after mergers, $r_{\mathrm{circ}} < r_{\mathrm{trap}}$ is satisfied in both emission scenarios, and super-Eddington accretion is realized due to the transition from the ADIOS to the ZEBRA flow. In this way, both the growth problem and the luminous flares implied in Graham et al. (2023) can be resolved.

Note that also in the ADIOS/ZEBRA prescription, a cavity is expected to form, and jet reorientation is therefore a necessary ingredient to produce electromagnetic flares accompanying GW events. Since the ram pressure of the wind is higher than the gas pressure of the AGN gas by a factor of $\gtrsim 10$ at the scale height of the AGN disk in both emission scenarios, we assume that a cavity forms around the BHs. On the other hand, the duty cycle of accretion phases would be high due to the weak ejection of circum-BH disks by the wind. This is because the wind is less decelerated by the AGN gas and is anisotropically launched. Then, the wind does not significantly erode the circum-BH disk (unlike the cocoon in T22). Due to the presence of the cavity, the jet reorientation is required to produce electromagnetic emission associated with mergers as depicted in Figure 1. Also note that although the super-Eddington accretion is assumed to always be established in the fiducial model (Section 2.1), the model in this paper also applies to the ADIOS/ZEBRA prescription.

Although we have focused on the interactions between the jet and AGN gas, those between the jet and the wind and between the jet and the circumbinary disk can also reproduce the properties of the optical (Graham et al. 2023) and gammaray (Connaughton et al. 2016; Tagawa et al. 2023b) flares, respectively, by assuming values for the parameters similar to those adopted in the shock cooling emission scenario (Table 2). It would be useful to further investigate these possibilities in the future.

3.4. Thermalization

Here, we discuss the validity of adopting the blackbody temperature in Equation (18). According to Equation (10) of Nakar & Sari (2010), to establish thermal equilibrium at the shock breakout in the shock cooling emission scenario (Table 2), the number of photons produced by free-free emission is insufficient by a factor of ~10-400 (except for pair 6 by a factor of \sim 3000). On the other hand, the blackbody temperature of the shocked gas at the shock breakout is so low $(\sim 10^{5}-10^{6} \text{ K})$ that bound-free emission produces more photons by a factor of $\gtrsim 100-3000$ at $\sim 3 Z_{\odot}$ compared to free-free emission (Sutherland & Dopita 1993). This factor further increases for higher-metallicity AGNs (Xu et al. 2018). Even though the breakout emission is not thermalized, since deeper shells of the shocked gas have more time (by a factor of \sim 10–3000) to create photons until the breakout, thermalization is expected in the shock cooling emission phase. For these reasons, we assume that a blackbody distribution is achieved for the emission in the shock cooling emission scenario. However, the assessment of the validity of this assumption, especially for high β_c cases such as pair 6, may need further investigation.

In the breakout emission scenario (Table 3), the blackbody temperature of the shocked gas is much higher due to the lower AGN density and the higher shock velocity. Then, bound–free emission is less dominant, and the emission in the breakout emission phase tends to be out of thermal equilibrium. In this scenario, we determine the radiation temperature (right panel of Figure 2) using the fitting formula derived in Equation (25) of Sapir et al. (2013), in which bound–free emission is not considered.

4. Tests of the Model

In the following, we discuss how our model can be tested by examining the distribution expected for the observable properties. From Sections 3.1 and 3.2, we see that values for each model parameter are distributed in a narrow range (Tables 2 and 3). We discuss whether this is because flares originating from merging BHs tend to have well-defined characteristic properties or because of observational selection effects in the way the search was conducted by Graham et al. (2023). Flares were searched with specific ranges of parameters, in particular with the rise time within 5–100 days, the decay time within 10–200 days, and the delay time from the GW detection in the interval of 0–200 days.

In order for electromagnetic flares to be found in association with BH mergers, BHs typically need to merge in bright AGNs. This is because most BH mergers reported by LIGO/Virgo/ KAGRA are found to merge at luminosity distances of several Gpc (Abbott et al. 2021). At such large distances, AGNs are easily missed unless they are bright. Indeed, the host SMBH masses for the flares reported by Graham et al. (2023) are $\gtrsim 10^8 M_{\odot}$, hence so massive that AGNs are rarely missed in AGN searches at the distances of the GW events. Also, assuming a luminosity distance of $d_L \sim 3$ Gpc, an SMBH mass of $10^8 M_{\odot}$, an Eddington ratio of ~ 1 , a bolometric correction of 5, and a fraction of the variable luminosity compared to the average luminosity of 0.1, the flux of variable flares in the AGN is $\sim 2 \times 10^{-13} \, \mathrm{erg \, s^{-1} \, cm^{-2}}$, which falls just above the sensitivity of ZTF $\sim 10^{-13} \, \mathrm{erg \, s^{-1} \, cm^{-2}}$. Conversely, it is difficult to find flares associated with BH mergers occurring in AGNs around less massive SMBHs through surveys for AGN variability.

We next estimate the detection rate of electromagnetic flares associated with BH mergers based on our scenario. If BH mergers actually produce electromagnetic flares as found in Graham et al. (2023), the rate of such flares is comparable to or less than the rate of BH mergers ($\sim O(10) \text{Gpc}^{-3} \text{yr}^{-1}$). If flares within \lesssim 3 Gpc are observable by the ZTF and all merging BHs produce electromagnetic flares, up to $N_{\rm BBH,3Gpc} \sim 300$ flares associated with BH mergers can be detected per year. On the other hand, we have estimated that a small fraction of BH mergers ($f_{\rm EM/BBH} \lesssim 0.02$) could accompany detectable electromagnetic flares in our model (see Section 4.1 in Paper I for discussions). Then, the seven flares discovered by Graham et al. (2023) are roughly consistent with the number of flares expected during LIGO/Virgo/KAGRA O3, which is estimated as $N_{\rm EM/GW,O3} \sim N_{\rm BBH,3Gpc} f_{\rm EM/BBH} t_{\rm O3} \lesssim 10$, where $t_{\rm O3} \sim 1.1$ is the duration of the O3 operation in units of years. Constraints on the frequency of flares, whose properties can be explained by emission from BHs, are hence useful to test our model. Here, note that dimmer, more frequent flares would be contributed by solitary BHs (Tagawa et al. 2023c).

4.1. Shock Cooling Emission

From Table 2, we note that there are moderate variations in $R_{\rm BH}$ and $T_{\rm BB}$ in the shock cooling emission scenario. To consider a possible test of this model, we discuss its dependence on the observed properties and the range of these properties for which the shock cooling emission scenario is inconsistent. If there are events with high or low $T_{\rm BB}$, extremely large or small $R_{\rm BH}$, or $R_{\rm BO}/R_{\rm diff}\geqslant 1$, such flares are inconsistent with the shock cooling emission scenario. However, the dependence of the variables $T_{\rm BB}$, $R_{\rm BH}$, and $R_{\rm BO}/R_{\rm diff}$ on the ratio of the observed parameters ($L_{\rm AGN}$, $L_{\rm obs}$, $m_{\rm BH}$, $M_{\rm SMBH}$, and $t_{\rm diff}$) over the adjustment parameters ($f_{\rm corr}$ and $f_{\rm jet/BHL}$) is similar to the dependence of $H_{\rm AGN}/R_{\rm BH}$ on the same ratio. For example, for $\beta_{\rm c}/\theta_0 < 1$, $H_{\rm AGN}/R_{\rm BH}$ depends on the observed properties as

$$\frac{H_{\text{AGN}}}{R_{\text{BH}}} = \frac{9^{4/3} L_{\text{AGN}}^2 L_{\text{obs}}^5 \kappa_{\text{ej}}^7 \theta_0^{2/3} f_{\text{corr}}^9}{2^{4/3} 4^4 \pi^7 f_{\text{jet/BHL}}^4 f_{\text{cons}}^2 c^{19} \alpha^2 \eta_{\text{rad}}^2 A^{4/3} G^3} \times \frac{1}{m_{\text{BH}}^{8/3} M_{\text{SMBH}}^{1/3} t_{\text{diff}}^{16/3}} \times L_{\text{obs}}^5 L_{\text{AGN}}^2 t_{\text{delay}}^{-16/3} m_{\text{BH}}^{-8/3} f_{\text{corr}}^9 f_{\text{jet/BHL}}^{-4}, \tag{29}$$

and $T_{\rm BB}$ depends as

$$T_{\rm BB} = \frac{9^{3/8} L_{\rm AGN}^{3/8} L_{\rm obs}^{11/8} \kappa_{\rm ej}^{3/2} f_{\rm corr}^{9/4}}{(4\pi)^{1/3} (32\pi^4)^{3/8} f_{\rm jet/BHL}^{9/8} f_{\rm cons}^{3/8} c^{9/2} A^{3/8} G^{3/4}} \times \frac{1}{\alpha^{3/8} \eta_{\rm rad}^{3/8} m_{\rm BH}^{3/4} t_{\rm diff}^{5/4} a^{3/8}} \times L_{\rm obs}^{11/8} L_{\rm AGN}^{3/8} t_{\rm delay}^{-5/4} m_{\rm BH}^{-3/4} f_{\rm corr}^{9/4} f_{\rm iet/BHI}^{-9/8} .$$
(30)

Then, if we adjust $f_{\rm corr}$ and $f_{\rm jet/BHL}$ so that $H_{\rm AGN}/R_{\rm BH}$ is consistent with a Shakura–Sunyaev disk, these parameters $(T_{\rm BB}, R_{\rm BH}, {\rm and}\ R_{\rm BO}/R_{\rm diff})$ also fall in a range of possible values (similar values to those derived in Table 2), even if events with wide ranges of observed parameters $(L_{\rm AGN}, L_{\rm obs}, m_{\rm BH}, M_{\rm SMBH}, {\rm and}\ t_{\rm diff})$ are observed. Thus, in this model, once $H_{\rm AGN}/R_{\rm BH}$ is adjusted to the value expected in the Shakura–Sunyaev model, $T_{\rm BB}, R_{\rm BH}, {\rm and}\ R_{\rm BO}/R_{\rm diff}$ are then characterized by realistic values, and the distribution of the observables becomes difficult to use as a further test of the model.

An interesting test of the model is the correlation between the delay time and the duration of the flare. This is because the delay time is comparable to the duration of a flare as long as $t_{\rm diff} \gg t_{\rm break}$, which is satisfied in pairs 1–12 (Table 2). To constrain the correlation coefficient, e.g., with an uncertainty of \lesssim 0.3 by the 95th percentile, \gtrsim 50 events need to be observed. Hence, more events will be very helpful as further diagnostics. Note that half of the pairs reported by Graham et al. (2023) are unreal, as a flare is associated with a few GW events; hence, we need to derive the correlation excluding the influence from false associations. Also, we derived the delay time using digitizer. In addition, the time dependence of the luminosity assumed by Graham et al. (2023) is different from that expected in the shock cooling emission. Thus, both the delay time and the duration suffer from significant uncertainties. If these timescales can be well constrained, the model can be tested for each event by comparing the delay time and the duration.

Another possible test is the detection of the breakout emission from the shocked gas preceding the shock cooling emission. In pairs 1–12, the duration and temperature of the breakout emission from the shocked gas range in the intervals $\sim 10-10^5$ s and 0.4–5 keV; thus, wide-field X-ray surveys, such as Einstein Probe (Yuan et al. 2015) and HiZ-GUNDAM (Yonetoku et al. 2020), will be useful to detect the early breakout emission (left panel of Figure 2). Assuming that the luminosity of the breakout emission is similar in magnitude to the jet power, the detectable distance is estimated to be

$$d_{\text{det}} = \left(\frac{L_{\text{j}}}{4\pi F_{\text{sen}}}\right)^{1/2}$$

$$\sim 1 \text{ Gpc} \left(\frac{L_{\text{j}}}{10^{46} \text{ erg s}^{-1}}\right)^{1/2} \left(\frac{F_{\text{sen}}}{10^{-11} \text{ erg s}^{-1} \text{ cm}^{-2}}\right)^{-1/2}, \quad (31)$$

where $F_{\rm sen}$ is the sensitivity of the facility. Here, the closest distance among the flares discovered by Graham et al. (2023) is ~Gpc. Since the duration of the breakout emission from the shocked gas is $\sim 10-10^5$ s in pairs 1–12 and the sensitivity of Einstein Probe (Yuan et al. 2015) and HiZ-GUNDAM is $F_{\rm sen} \sim 10^{-11} \, {\rm erg \, s^{-1} \, cm^{-2}}$ for $t_{\rm int} \sim 10^4 \, {\rm s}$, events at the luminosity distance of \sim Gpc can be detected if $L_{\rm j} \gtrsim 10^{46} \, {\rm erg \, s^{-1}}$. If both the breakout emission and the shock cooling emission are detected from the same AGN, it can be a robust test of this model.

It is notable that in the shock cooling model, the color keeps evolving to redder in all pairs (Figure 3(d)). The $m_g - m_r$ evolves by ~ 0.4 in 50 days. Such mild evolution of the color can be a strong test of this model. On the other hand, for nonthermal emission from the breakout of the jet head, the color is expected to be unchanged. Note that the colors are presented for pair 3 in Figure 2 of Graham et al. (2020), revealing almost no evolution. However, due to the contamination from the host AGN emission, any color evolution is likely difficult to constrain. To derive the color evolution more precisely, observations at additional frequencies, e.g., by ULTRASAT (black lines of Figure 3(c)), would also be useful. Hence, when available, the evolution of the color will be an additional diagnostic in future observations.

4.2. Breakout Emission

Next, we discuss ways to test the breakout emission scenario. To do this, we first present the dependence of physical quantities on observables as

$$\beta_{\rm h} \propto \theta_0^{-12/11} f_{\rm jet/BHL}^{3/11} f_{\rm corr}^{-3/11} t_{\rm delay}^{-3/11} t_{\rm duration}^{1/22},$$
 (32)

$$\beta_{\rm h} \propto \theta_0^{-12/11} f_{\rm jet/BHL}^{3/11} f_{\rm corr}^{-3/11} t_{\rm delay}^{-3/11} t_{\rm duration}^{1/22}, \tag{32}$$

$$H_{\rm AGN} \propto \theta_0^{-12/11} f_{\rm jet/BHL}^{3/11} f_{\rm corr}^{-14/11} t_{\rm delay}^{8/11} t_{\rm duration}^{1/22}, \tag{33}$$

$$\rho_{\rm AGN} \propto \theta_0^{24/11} f_{\rm jet/BHL}^{-6/11} f_{\rm corr}^{6/11} t_{\rm delay}^{6/11} t_{\rm duration}^{-12/22}, \tag{34}$$

$$R_{\rm BH} \propto \theta_0^{-8/11} f_{\rm jet/BHL}^{2/11} M_{\rm SMBH}^{1/3} f_{\rm corr}^{-2/11} t_{\rm delay}^{-2/11} t_{\rm duration}^{4/22},$$
 (35)

$$L_{\rm j} \propto \theta_0^{8/11} f_{\rm jet/BHL}^{9/11} f_{\rm corr}^{-9/11} t_{\rm delay}^{13/11} t_{\rm duration}^{-19/22},$$
 (36)

$$\dot{M}_{\rm inflow} \propto \theta_0^{4/11} f_{\rm jet/BHL}^{-1/11} m M_{\rm SMBH}^{1/2} f_{\rm corr}^{-17/11} t_{\rm delay}^{23/11} t_{\rm duration}^{-13/22}$$
. (37)

For the breakout emission from the jet head, if the shocked gas becomes relativistic ($\beta_h \gtrsim 0.8$), the probability of observing nonthermal emission is significantly reduced due to the relativistic beaming effects, the shift of the minimum energy, and the time dilution (as shown in Figure 3(b) of Paper I).

Thus, if the shock is relativistic, the breakout emission is presumably not observed by current facilities, such as ZTF. Since β_h is estimated to be ~ 0.2 –0.4 for the observed flares, if β_h is higher by a factor of \sim 3 compared to our estimates, flares cannot be explained by breakout emission. $\beta_h \gtrsim 0.8$ is satisfied in all the pairs if events with delay times of $t_{\rm delay} \lesssim 2$ days are found. Note that this is not compensated by f_{corr} and $f_{\text{jet/BHL}}$ (as in the shock cooling emission scenario). This is because β_h is reduced only by a factor of ~ 1.1 by enhancing $f_{\rm corr}$ to the maximum value ($\sim 1/\theta_0$). Also, if $f_{\text{jet/BHL}}$ is reduced to lower $\beta_{\rm h}$, $f_{\rm op/kin}$ becomes larger than 1, which violates another requirement for the model. If associations between the flares and GWs are due to random coincidence, the delay time is expected to be distributed uniformly in the range of 0-200 days. Assuming a uniform distribution, we can test the breakout emission scenario at the $\sim 1\sigma$ and $\sim 2\sigma$ levels after discovering \$\ge 100\$ and \$\ge 300\$ events, respectively, by checking if there are events with $t_{\rm delay} \lesssim 2$ days. If we find optical flares with $t_{\rm delay} \lesssim 2$ days, the breakout emission scenario is

If t_{duration} is enhanced by 1 order of magnitude, the jet power is reduced by a similar factor, and the fraction of the optical luminosity to the jet power exceeds 1 for pairs 1–3, 6, 11, and 12, and then the breakout emission scenario becomes inconsistent for these pairs. However, the enhancement of L_i due to long t_{duration} can be compensated by $f_{\text{jet/BHL}}$ and f_{corr} up to about a factor of \sim 10, which is limited by the requirement for β_h (≤ 0.8) as discussed above. Hence, the model is not well tested by t_{duration} .

Currently, the properties of the observed flares satisfy the conditions required for the breakout emission scenario. To be consistent with this scenario, the delay time should not be shorter than ~ 2 days, and the color of the flares should be distributed in a narrow range as discussed in Section 3.1. Thus, to test whether there are flares with properties that are inconsistent with the breakout emission scenario, more events will need to be observed.

When considering the emission from the jet head, we ignored the acceleration of shocked gas in the lateral direction with respect to the shock surface (Matzner et al. 2013; Irwin et al. 2021). In nearly spherically symmetric geometry, the shocked gas that expanded earlier can obscure the breakout emission from gas that shocked later due to the lateral acceleration, thus reducing the luminosity and increasing the duration of the early emission. On the other hand, in the planar geometry considered in our model, such obscuration may be avoided, since the shocked gas may not cover the later breakout emission (Linial & Sari 2019). To investigate the influence of this acceleration, radiative-hydrodynamical simulations are desirable.

5. Conclusions

In this paper, we have presented the properties of emission from shocks emerging from collisions between AGN gas and a jet launched from a merger remnant BH in an AGN disk. Our model includes the evolution throughout the shock breakout and subsequent cooling emission phases. We then applied this model to the candidate flares reported in Graham et al. (2023). Our results are summarized as follows.

1. We fit the characteristic features of all of the events with both emission processes. Both processes could fit each

- observation, suggesting that such fits may themselves be insufficient to rule out the AGN origin for the flares. The reconstructed parameters might then be indicative of the selection algorithm determining the false-alarm rate of associations.
- 2. While both processes could be made consistent with the observed events with appropriate parameter selection, we found that the implied merger distance from the central SMBH is markedly different for the two processes. Specifically, shock cooling emission can explain the observed properties if the mergers happen $R_{\rm BH} \sim 0.06$ –0.3 pc from the SMBH, which is consistent with the locations of AGN-assisted merger models (e.g., Tagawa et al. 2020b). On the other hand, breakout emission would require a much larger distance of $R_{\rm BH} \sim 1$ –8 pc to explain the observed flare duration. This may be possible for mergers in AGNs with high SMBH masses, in which migration is inefficient (e.g., Perna et al. 2021b).
- 3. Follow-up observations could help further constrain the reconstructed parameters of the events. X-ray observations would have to be made prior to the optical detection, which likely requires future wide-field surveys. In addition, follow-up observations determining the spectral evolution of the electromagnetic flares would be important.
- 4. To reproduce the high luminosity of the electromagnetic flares without significant growth of the stellar-mass BHs and also without making the association of electromagnetic flares and GW events exceedingly rare, we outlined a picture in which ~Eddington-limited accretion in ADIOS flows transitions to hyperaccreting ZEBRA flows at the time of the mergers.

Acknowledgments

We thank Kazumi Kashiyama for reminding us of the importance of the rapid growth of accreting BHs (Tagawa et al. 2022) in the context of this study. H.T. was supported by the National Key R&D Program of China (grant No. 2021YFC2203002). S.S.K. was supported by Japan Society for the Promotion of Science (JSPS) KAKENHI grant Nos. 22K14028, 21H04487, and 23H04899 and the Tohoku Initiative for Fostering Global Researchers for Interdisciplinary Sciences (TI-FRIS) of MEXT's Strategic Professional Development Program for Young Researchers. Z.H. was supported by NASA grant 80NSSC22K0822 and NSF grant AST-2006176. R.P. acknowledges support by NSF award AST-2006839. I.B. acknowledges the support of the Alfred P. Sloan Foundation and NSF grants PHY-1911796 and PHY-2110060.

ORCID iDs

Hiromichi Tagawa https://orcid.org/0000-0002-5674-0644 Shigeo S Kimura https://orcid.org/0000-0003-2579-7266 Zoltán Haiman https://orcid.org/0000-0003-3633-5403 Rosalba Perna https://orcid.org/0000-0002-3635-5677

References

```
Abbott, R., Abbott, T. D., Abraham, S., et al. 2021, PhRvX, 11, 021053 Abbott, R., Abbott, T. D., Acernese, F., et al. 2023, PhRvX, 13, 041039 Acernese, F., Agathos, M., Agatsuma, K., et al. 2015, CQGra, 32, 024001 Akutsu, T., Ando, M., Arai, K., et al. 2021, PTEP, 2021, 05A101
```

```
Antonini, F., Gieles, M., Dosopoulou, F., & Chattopadhyay, D. 2023,
  MNRAS, 522, 466
Antonini, F., Toonen, S., & Hamers, A. S. 2017, ApJ, 841, 77
Arca Sedda, M., Naoz, S., & Kocsis, B. 2023, Univ, 9, 138
Arnett, W. D. 1980, ApJ, 237, 541
Ashton, G., Ackley, K., Hernandez, I. M., & Piotrzkowski, B. 2021, CQGra,
  38, 235004
Bagoly, Z., Szécsi, D., Balázs, L. G., et al. 2016, A&A, 593, L10
Banerjee, S. 2017, MNRAS, 467, 524
Barack, L., Cardoso, V., Nissanke, S., et al. 2019, CQGra, 36, 143001
Bartos, I., Kocsis, B., Haiman, Z., & Márka, S. 2017, ApJ, 835, 165
Bartos, I., Rosswog, S., Gayathri, V., et al. 2023, arXiv:2302.10350
Begelman, M. C., & Armitage, P. J. 2023, MNRAS, 521, 5952
Begelman, M. C., & Silk, J. 2023, MNRAS, 526, L94
Begelman, M. C., & Volonteri, M. 2017, MNRAS, 464, 1102
Belczynski, K., Daniel, E. H., Bulik, T., & O'Shaughnessy, R. 2016, Natur,
  534, 512
Bellovary, J. M., Mac Low, M.-M., McKernan, B., & Ford, K. E. S. 2016,
   ApJL, 819, L17
Berger, E. 2014, ARA&A, 52, 43
Blandford, R. D., & Begelman, M. C. 1999, MNRAS, 303, L1
Blandford, R. D., & Znajek, R. L. 1977, MNRAS, 179, 433
Boekholt, T. C. N., Rowan, C., & Kocsis, B. 2023, MNRAS, 518, 5653
Bromberg, O., Nakar, E., Piran, T., & Sari, R. 2011, ApJ, 740, 100
Burrows, D. N., Hill, J. E., Nousek, J. A., et al. 2005, SSRv, 120, 165
Calderón Bustillo, J., Leong, S. H. W., Chandra, K., McKernan, B., &
  Ford, K. E. S. 2021, arXiv:2112.12481
Chen, K., Ren, J., & Dai, Z.-G. 2023a, ApJ, 948, 136
Chen, Y.-X., Jiang, Y.-F., Goodman, J., & Ostriker, E. C. 2023b, ApJ,
  948, 120
Choksi, N., Chiang, E., Fung, J., & Zhu, Z. 2023, MNRAS, 525, 2806
Collin, S., & Zahn, J. P. 2008, A&A, 477, 419
Connaughton, V., Burns, E., Goldstein, A., et al. 2016, ApJL, 826, L6
Coughlin, E. R., & Begelman, M. C. 2014, ApJ, 781, 82
de Mink, S. E., & King, A. 2017, ApJL, 839, L7
DeLaurentiis, S., Epstein-Martin, M., & Haiman, Z. 2023, MNRAS, 523,
  1126
Derdzinski, A., D'Orazio, D., Duffell, P., Haiman, Z., & MacFadyen, A. 2021,
   MNRAS, 501, 3540
Derdzinski, A., & Mayer, L. 2023, MNRAS, 521, 4522
Derdzinski, A. M., D'Orazio, D., Duffell, P., Haiman, Z., & MacFadyen, A.
  2019, MNRAS, 486, 2754
Dominik, M., Belczynski, K., Fryer, C., et al. 2012, ApJ, 759, 52
Duras, F., Bongiorno, A., Ricci, F., et al. 2020, A&A, 636, A73
Ford, K. E. S., & McKernan, B. 2022, MNRAS, 517, 5827
Fragione, G., & Kocsis, B. 2018, PhRvL, 121, 161103
Fragione, G., & Kocsis, B. 2019, MNRAS, 486, 4781
Gayathri, V., Healy, J., Lange, J., et al. 2022, NatAs, 6, 344
Gayathri, V., Wysocki, D., Yang, Y., et al. 2023, ApJL, 945, L29
Gayathri, V., Yang, Y., Tagawa, H., Haiman, Z., & Bartos, I. 2021, ApJL,
  920, L42
Generozov, A., & Perets, H. B. 2023, MNRAS, 522, 1763
Georgiev, I. Y., Boker, T., Leigh, N., Lutzgendorf, N., & Neumayer, N. 2016,
      IRAS, 457, 2122
Goodman, J., & Tan, J. C. 2004, ApJ, 608, 108
Gottlieb, O., Nakar, E., & Piran, T. 2018, MNRAS, 473, 576
Graham, M. J., Ford, K. E. S., McKernan, B., et al. 2020, PhRvL, 124,
  251102
Graham, M. J., McKernan, B., Ford, K. E. S., et al. 2023, ApJ, 942, 99
Grishin, E., Bobrick, A., Hirai, R., Mandel, I., & Perets, H. B. 2021, MNRAS,
  507, 156
Grishin, E., Gilbaum, S., & Stone, N. C. 2023, arXiv:2307.07546
Hada, K., Doi, A., Wajima, K., et al. 2018, ApJ, 860, 141
Hada, K., Kino, M., Doi, A., et al. 2013, ApJ, 775, 70
Haiman, Z., Kocsis, B., & Menou, K. 2009, ApJ, 700, 1952
Hamidani, H., & Ioka, K. 2023, MNRAS, 524, 4841
Harrison, F. A., Craig, W. W., Christensen, F. E., et al. 2013, ApJ, 770, 103
Hopkins, P. F., & Quataert, E. 2010, MNRAS, 407, 1529
Irwin, C. M., Linial, I., Nakar, E., Piran, T., & Sari, R. 2021, MNRAS,
Ivezić, Ž., Kahn, S., Tyson, J. A., et al. 2019, ApJ, 873, 111
Izumi, T., Wada, K., Imanishi, M., et al. 2023, Sci, 382, 554
Jansen, F., Lumb, D., Altieri, B., et al. 2001, A&A, 365, L1
Kimura, S. S., Murase, K., & Bartos, I. 2021, ApJ, 916, 111
Kinugawa, T., Inayoshi, K., Hotokezaka, K., Nakauchi, D., & , T. N. 2014,
   MNRAS, 442, 2963
```

```
Kitaki, T., Mineshige, S., Ohsuga, K., & Kawashima, T. 2021, PASJ, 73,
Kormendy, J., & Ho, L. C. 2013, ARA&A, 51, 511
Kumamoto, J., Fujii, M. S., & Tanikawa, A. 2018, MNRAS, 486, 3942
Lazzati, D., Soares, G., & Perna, R. 2022, ApJL, 938, L18
Levin, Y., & Beloborodov, A. M. 2003, ApJL, 590, L33
Li, J., Dempsey, A. M., Li, H., Lai, D., & Li, S. 2023, ApJL, 944, L42
Li, J., Lai, D., & Rodet, L. 2022, ApJ, 934, 154
Li, Y.-P., Dempsey, A. M., Li, S., Li, H., & Li, J. 2021, ApJ, 911, 124
LIGO Scientific Collaboration, Assi, J., Abbott, B P., et al. 2015, CQGra, 32,
Linial, I., & Sari, R. 2019, PhFl, 31, 097102
Liska, M., Hesp, C., Tchekhovskoy, A., et al. 2018, MNRAS, 474, L81
Liska, M., Hesp, C., Tchekhovskoy, A., et al. 2021, MNRAS, 507, 983
Martinez, M. A. S., Rodriguez, C. L., & Fragione, G. 2022, ApJ, 937, 78
Matzner, C. D. 2003, MNRAS, 345, 575
Matzner, C. D., Levin, Y., & Ro, S. 2013, ApJ, 779, 60
McKernan, B., Ford, K. E. S., Bartos, I., et al. 2019, ApJL, 884, L50
McKernan, B., Ford, K. E. S., Bellovary, J., et al. 2018, ApJ, 866, 66
Michaely, E., & Perets, H. B. 2019, ApJL, 887, L36
Milosavljević, M., & Loeb, A. 2004, ApJL, 604, L45
Miralda-Escudé, J., & Kollmeier, J. A. 2005, ApJ, 619, 30
Mizuta, A., & Ioka, K. 2013, ApJ, 777, 162
Morag, J., Sapir, N., & Waxman, E. 2023, MNRAS, 522, 2764
Morton, S. L., Rinaldi, S., Torres-Orjuela, A., et al. 2023, PhRvD, 108, 123039
Nakar, E., & Piran, T. 2017, ApJ, 834, 28
Nakar, E., & Sari, R. 2010, ApJ, 725, 904
Narayan, R., Chael, A., Chatterjee, K., Ricarte, A., & Curd, B. 2022, MNRAS,
O'Leary, R. M., Meiron, Y., & Kocsis, B. 2016, ApJL, 824, L12
Ostriker, J. P. 1983, ApJ, 273, 99
Palmese, A., Fishbach, M., Burke, C. J., Annis, J., & Liu, X. 2021, ApJL,
   914, L34
Panaitescu, A., & Kumar, P. 2001, ApJL, 560, L49
Perna, R., Lazzati, D., & Cantiello, M. 2021a, ApJL, 906, L7
Perna, R., Tagawa, H., Haiman, Z., & Bartos, I. 2021b, ApJ, 915, 10
Perna, R., Wang, Y.-H., Farr, W. M., Leigh, N., & Cantiello, M. 2019, ApJL,
  878, L1
Piro, A. L., Haynie, A., & Yao, Y. 2021, ApJ, 909, 209
Planck Collaboration, Ade, P. A. R., Aghanim, N., et al. 2016, A&A, 594,
Polko, P., & McKinney, J. C. 2017, MNRAS, 464, 2660
Portegies Zwart, S. F., & McMillan, S. L. W. 2000, ApJ, 528, L17
Prasad, C., Wang, Y., Perna, R., Ford, K. E. S., & McKernan, B. 2023,
  arXiv:2310.00020
Qian, K., Li, J., & Lai, D. 2024, ApJ, 962, 143
Rasskazov, A., & Kocsis, B. 2019, ApJ, 881, 20
Ray, M., Lazzati, D., & Perna, R. 2023, MNRAS, 521, 4233
Rodriguez, C. L., Chatterjee, S., & Rasio, F. A. 2016, PhRvD, 93, 084029
Rodríguez-Ramírez, J. C., Bom, C. R., Fraga, B., & Nemmen, R. 2024,
      IRAS, 527, 6076
Romero-Shaw, I., Lasky, P. D., & Thrane, E. 2022, ApJ, 940, 171
Romero-Shaw, I. M., Gerosa, D., & Loutrel, N. 2023, MNRAS, 519, 5352
Romero-Shaw, I. M., Lasky, P. D., Thrane, E., & Calderon Bustillo, J. 2020,
```

ApJL, 903, L5

```
Rossi, E. M., Lodato, G., Armitage, P. J., Pringle, J. E., & King, A. R. 2010,
  MNRAS, 401, 2021
Rowan, C., Boekholt, T., Kocsis, B., & Haiman, Z. 2023, MNRAS, 524, 2770
Rowan, C., Whitehead, H., Boekholt, T., Kocsis, B., & Haiman, Z. 2024,
  MNRAS, 527, 10448
Rozner, M., Generozov, A., & Perets, H. B. 2023, MNRAS, 521, 866
Ruffert, M., & Anzer, U. 1995, A&A, 295, 108
Samsing, J., Bartos, I., D'Orazio, D. J., et al. 2022, Natur, 603, 237
Samsing, J., MacLeod, M., & Ramirez-Ruiz, E. 2014, ApJ, 784, 71
Sapir, N., Katz, B., & Waxman, E. 2013, ApJ, 774, 79
Sapir, N., & Waxman, E. 2017, ApJ, 838, 130
Scott, N., & Graham, A. W. 2013, ApJ, 763, 76
Shvartzvald, Y., Waxman, E., Gal-Yam, A., et al. 2024, ApJ, 964, 74
Shakura, N. I., & Sunyaev, R. A. 1973, A&A, 24, 337
Silsbee, K., & Tremaine, S. 2017, ApJ, 836, 39
Spera, M., Mapelli, M., Giacobbo, N., et al. 2019, MNRAS, 485, 889
Spergel, D., Gehrels, N., Baltay, C., et al. 2015, arXiv:1503.03757
Stone, N. C., Metzger, B. D., & Haiman, Z. 2017, MNRAS, 464, 946
Sutherland, R. S., & Dopita, M. A. 1993, ApJS, 88, 253
Tagawa, H., Haiman, Z., Bartos, I., & Kocsis, B. 2020a, ApJ, 899, 26 Tagawa, H., Haiman, Z., & Kocsis, B. 2020b, ApJ, 898, 25
Tagawa, H., Kimura, S. S., & Haiman, Z. 2023a, ApJ, 955, 23
Tagawa, H., Kimura, S. S., Haiman, Z., et al. 2022, ApJ, 927, 41
Tagawa, H., Kimura, S. S., Haiman, Z., Perna, R., & Bartos, I. 2023b, ApJ,
  950. 13
Tagawa, H., Kimura, S. S., Haiman, Z., Perna, R., & Bartos, I. 2023c, ApJL,
Tagawa, H., Kocsis, B., Haiman, Z., et al. 2021a, ApJ, 908, 194
Tagawa, H., Kocsis, B., Haiman, Z., et al. 2021b, ApJL, 907, L20
Tagawa, H., Kocsis, B., & Saitoh, R. T. 2018, PhRvL, 120, 261101
Tanigawa, T., Ohtsuki, K., & Machida, M. N. 2012, ApJ, 747, 47
Tanigawa, T., & Tanaka, H. 2016, ApJ, 823, 48
Tanigawa, T., & Watanabe, S.-i. 2002, ApJ, 580, 506
Tanikawa, A., Yoshida, T., Kinugawa, T., et al. 2022, ApJ, 926, 83
Tchekhovskoy, A., Narayan, R., & McKinney, J. C. 2010, ApJ, 711, 50
Thompson, T. A., Quataert, E., & Murray, N. 2005, ApJ, 630, 167
Wang, J.-M., Liu, J.-R., Ho, L. C., & Du, P. 2021a, ApJL, 911, L14
Wang, J.-M., Liu, J.-R., Ho, L. C., Li, Y.-R., & Du, P. 2021b, ApJL, 916, L17
Wang, Y., Zhu, Z., & Lin, D. N. C. 2024, MNRAS, 528, 4958
Wang, Y.-H., Lazzati, D., & Perna, R. 2022, MNRAS, 516, 5935
Whitehead, H., Rowan, C., Boekholt, T., & Kocsis, B. 2023a, arXiv:2309.
  11561
Whitehead, H., Rowan, C., Boekholt, T., & Kocsis, B. 2023b, arXiv:2312.
  14431
Xin, C., Haiman, Z., Perna, R., Wang, Y., & Ryu, T. 2024, ApJ, 961, 149
Xu, F., Bian, F., Shen, Y., et al. 2018, MNRAS, 480, 345
Yang, Y., Bartos, I., Fragione, G., et al. 2022, ApJL, 933, L28
Yonetoku, D., Mihara, T., Doi, A., et al. 2020, Proc. SPIE, 11444, 114442Z
Yuan, C., Murase, K., Guetta, D., et al. 2022, ApJ, 932, 80
Yuan, F., & Narayan, R. 2014, ARA&A, 52, 529
Yuan, W., Zhang, C., Feng, H., et al. 2015, arXiv:1506.07735
Zhou, Z.-H., & Wang, K. 2023, ApJL, 958, L12
Zhu, J.-P. 2024, MNRAS, 528, L88
Zhu, J.-P., Wang, K., & Zhang, B. 2021a, ApJL, 917, L28
Zhu, J.-P., Yang, Y.-P., Zhang, B., et al. 2021b, ApJL, 914, L19
Zhu, J.-P., Zhang, B., Yu, Y.-W., & Gao, H. 2021c, ApJL, 906, L11
```